Die approbierte Originalversion dieser Diplom-/Masterarbeit ist in der Hauptbibliothek der Technischen Universität Wien aufgestellt und zugänglich.
http://www.ub.tuwien.ac.at

The approved original version of this diploma or master thesis is available at the main library of the Vienna University of Technology.
http://www.ub.tuwien.ac.at/eng

Unterschrift des Betreuers

HEPHY Institut für Hochenergiephysik

TU WIEN TECHNISCHE UNIVERSITÄT WIEN

DIPLOMARBEIT

Performance Studies of Silicon Strip Sensors for the Phase-II Upgrade of the CMS Tracker

ausgeführt am Institut für Hochenergiephysik
der Österreichischen Akademie der Wissenschaften

unter der Anleitung von

Privatdoz. Dipl.-Ing. Dr.techn. Christoph SCHWANDA

und

Univ.Lektor Dipl.-Ing. Dr.techn. Thomas BERGAUER

durch

Peter PAULITSCH, BSc BSc
Pobersacherstraße 214,
9710 Feistritz an der Drau

Wien, am 26.3.2018

Unterschrift

Kurzfassung

Um 2025 wird der LHC (Large Hadron Collider) zum High-Luminosity LHC ausgebaut. Die Luminosität wird um den Faktor 5 bis 10 erhöht, bis auf 10^{35} $cm^{-2}s^{-1}$. Daraus ergeben sich neue Anforderungen für die Experimente wie dem Compact Muon Solenoid (CMS), wo auch aufgrund von Alterungserscheinungen (Strahlenschäden) die derzeit eingebauten Si-Sensoren des Spurdetektors („Tracker“) in Zukunft nicht weiter eingesetzt werden können. Darum, und um die neuen Herausforderungen wie stärkere Strahlungsdosen (durch die Erhöhung der Kollisionsrate) und höhere Datenraten zu bewerkstelligen, muss der CMS Tracker neu gebaut werden. Prototypen von dazu notwendigen Siliziumstreifendetektoren werden von den Firmen Infineon und Hamamatsu hergestellt. Diese müssen von Instituten wie dem HEPHY für den Einsatz qualifiziert werden.
Im Zuge dieser Diplomarbeit führte ich Messungen an diesen Sensor-Prototypen mit Protonen (64 bis 252 MeV) am MedAustron und mit Elektronen (5.6 GeV) am Deutschen Elektronen-Synchrotron (DESY) in Form von Testbeams durch, analysierte die Daten und führte Performance- und Qualitätstests durch. Diese umfassten IV-Charakteristika, Rauschanteil, Cluster-Analysen, Beamprofil-Messungen, Effizienz- und Energiemessungen. In Vorbereitung auf die Testbeams testete ich neue Trigger-Szintillatoren bezüglich Dunkelrate und Effizienz, des Weiteren das Streifensensor-System mittels einer radioaktiven Quelle und einem Laser-Testaufbau am Institut für Hochenergiephysik (HEPHY). Beim ersten Testbeam am MedAustron überstiegen hohe Teilchenraten (bis 10^{10}/s) die maximal mögliche Prozessierungsrate des Sensorsystems. Des Weiteren dominierten Occupancy und Pile-Up-Effekte das Signal und verfälschten die gemessene Energiedeposition. Während des Testbeams wurde beobachtet, dass die Spannungsversorgung des Streifensensors in Compliance ging, was zu Spannungseinbrüchen führte. Nach Änderungen im Beschleunigersystem durch das MedAustron-Personal waren niedrigere Teilchenraten (10^5/s) für den zweiten Testbeam verfügbar. Diese Maßnahmen, ergänzt durch Optimierungen im Aufbau, führten zu einer stabilen Spannungsversorgung und die Auswertung der Daten zu einer exzellenten Übereinstimmung des ermittelten Bremsvermögens mit Referenzdaten.
Zukünftige Testbeams erfordern umfangreiche Vorbereitungen in Bezug auf Funktionstests, Standardisierung und Simulation um frühzeitig Designschwächen zu identifizieren. Um in Zukunft bessere Energieauflösungen zu erzielen, ist seitens MedAustron eine scharf definierte Teilchenratenkontrolle essentiell, ebenso wie Monitoring des Sensorstromverbrauches in hoher Zeitauflösung. Falls ein Bedarf an Niedrigenergie-Testbeams besteht, ist es essentiell das nichtlineare Verhalten des ALiBaVa-Systems zu analysieren, und eventuell darauf aufbauend den Algorithmus der Analysesoftware zu erweitern. Weitere Maßnahmen sollten den erweiterten Schutz gegen elektromagnetische Störungen umfassen. Möglicherweise kann auch ein passendes Modell gefunden werden um das elektronische Rauschen zu beschreiben und um letztendlich das SNR zu erhöhen.

Abstract

In 2025, the LHC (Large Hadron Collider) will be upgraded to the High-Luminosity LHC. The luminosity will be enhanced by a factor of 5 to 10, up to $10^{35}\,\mathrm{cm^{-2}s^{-1}}$. This leads to new challenges for experiments such as the Compact Muon Solenoid (CMS), which is already afflicted by aging effects (radiation damages). Therefore the currently installed silicon sensors of the track detector ("Tracker") have to be replaced, furthermore to carry out higher radiation doses (through raised collision rates) and increased data rates. The prototypes of the new sensors are provided by the vendors Infineon and Hamamatsu. These have to be qualified for application by institutes like the HEPHY.
For this diploma thesis, I did testbeam measurements on these sensors using protons (64 to 252 MeV) at MedAustron and electrons (5.6 GeV) at Deutsches Elektronen-Synchrotron (DESY), analyzed the data and utilized performance and quality evaluation. These methods include IV characteristics, noise contribution, cluster analysis, beam profile measurement, efficiency and energy measurements. In preparation for the testbeams, I tested new trigger scintillators to determine dark rates and efficiency and the strip sensor system using a radioactive source and a laser test stand at the Institute of High Energy Physics (HEPHY).
At the MedAustron's first testbeam, high particle rates (up to 10^{10}/s) exceeded the sensor system's processing rate. Occupancy and pile-up effects dominated the signal and distorted measured energy depositions. During the testbeam, the bias voltage supply of the strip sensor showed compliance, leading to voltage drops. After changes made to the accelerator by MedAustron staff, lower particle rates (10^{5}/s) were available at the second testbeam. These actions, complemented by optimizations in the setup, lead to stable power supply and analysis showed excellent conformity of measured stopping power to reference data.
Prospective testbeams require extensive preparations in terms of functionality tests, standardization and simulation in advance to identify design flaws. For achieving better energy resolution in future, well-defined particle rate control by MedAustron is essential, as well as high time-resolved monitoring the current consumption of the sensor. If there is a demand for low-energy testbeams, it is essential to analyze the non-linear gain behavior in the upper energy deposition range of the ALiBaVa system. Based on that, one may eventually extend the analysis software algorithm. Further procedures should cover protection against electromagnetic interference. Perhaps it will be possible to find an appropriate model to characterize electronic noise contribution to improve SNR.

Acknowledgements

I would first like to thank my head supervisor, Privatdoz. Dipl.-Ing. Dr. Christoph Schwanda of the Austrian Academy of Sciences. He consistently allowed this paper to be my own work, but steered me in the right direction when I left the path of scientific precision.
Furthermore I would like to thank my other supervisor, Univ.-Lektor Dipl.-Ing. Dr. Thomas Bergauer for his support and introduction to the topic and fundamental physics. His encouragement and immediate help with emerging problems made it possible to master this thesis efficiently. He provided me a broad spectrum of tasks and assignments which resulted in a good overview of the topic.
A very special gratitude goes out to all staff at HEPHY: Johannes Grossmann MSc, Dipl.-Ing. Viktoria Hinger and Dr. Axel König MSc for giving excellent introductions in the underlying physics and teaching me how to use the required devices and software and furthermore to Dipl.-Ing. Dominic Blöch, Wolfgang Brandner, Dipl.-Ing. Dr. Marko Dragicevic, Elias Pree MSc, Dipl.-Ing. Stefan Schultschik, Dipl.-Ing. Dr. Manfred Valentan and Dipl.-Ing. Hao Yin who assisted me with useful tips, clear explanations and auxiliary work.
I would also like to acknowledge the personnel from MedAustron, in particular Univ.Ass. Dipl.-Ing. Dr. Albert Hirtl, Univ.Ass. Dipl.-Ing. Alexander Burker and Felix Ulrich-Pur BSc for helping and providing complementary tasks for the work.
With a special mention to Daniel Schell MSc and Marius Metzler MSc (both from Karlsruhe Institute of Technology), I would like to thank the people providing cooperative work at the DESY testbeam.
I want to express my gratitude to my close friends Dipl.-Ing. (FH) Roland Rittchen MSc MSc, Daniel Steiner MSc and also to my girlfriend Lisa Pirker for proofreading.
Last but not least, I would like to thank my family: My sister Dr. Andrea Paulitsch-Buckingham for her proofreading and my parents VR Mag. Dr. Peter Paulitsch and VOL Marina Paulitsch, for providing financial and motivational support to ensure the completion of this thesis.

Contents

1. Introduction and Background **8**
- 1.1. Motivation . . . 8
- 1.2. LHC - Large Hadron Collider . . . 9
- 1.3. CMS experiment . . . 11
  - 1.3.1. Subsystems . . . 12
  - 1.3.2. Phase-II Upgrade . . . 15
- 1.4. MedAustron . . . 16
- 1.5. DESY - Deutsches Elektronen-Synchrotron . . . 17

2. Theory of Particle Detectors **20**
- 2.1. Interaction of charged particles with matter . . . 20
  - 2.1.1. Excitation of electrons: Scintillation . . . 20
  - 2.1.2. Bremsstrahlung . . . 20
  - 2.1.3. Ionizing effects . . . 22
  - 2.1.4. Gaussian distribution . . . 26
  - 2.1.5. Landau distribution . . . 26
  - 2.1.6. Vavilov distribution . . . 27
- 2.2. Scintillation detector systems . . . 28
  - 2.2.1. Scintillators . . . 29
  - 2.2.2. Photomultiplier tubes . . . 29
  - 2.2.3. NIM electronics . . . 29
- 2.3. Semiconductor physics and silicon detectors . . . 30
  - 2.3.1. Drift . . . 31
  - 2.3.2. Diffusion . . . 32
  - 2.3.3. Doping and p-n junction . . . 33
  - 2.3.4. Signal generation, analog readout and signal processing . . . 34
  - 2.3.5. Segmentation and silicon strip sensors . . . 35
  - 2.3.6. Charge sharing and eta value . . . 35

3. Experimental Setup and Preparatory Tests at HEPHY **37**
- 3.1. Principles of testbeam setups . . . 37
  - 3.1.1. Telescope . . . 37
  - 3.1.2. Triggering and data acquisition . . . 37
- 3.2. Experimental setting . . . 38
  - 3.2.1. Scintillator system . . . 38
  - 3.2.2. Strip sensor readout: The ALiBaVa system . . . 39

3.3. Preparatory scintillator tests . . . 41
3.3.1. Dark rate determination . . . 41
3.3.2. Radioactive source tests with ^{90}Sr . . . 42
3.4. Preparatory strip sensor tests . . . 44
3.4.1. IV characteristics . . . 45
3.4.2. Radioactive source tests . . . 46
3.4.3. Laser tests in the clean room . . . 46
3.5. Proton testbeam 1 (TB 1) at MedAustron . . . 48
3.6. Proton testbeam 2 (TB 2) at MedAustron . . . 49
3.7. Electron testbeam at DESY . . . 51

4. Testbeam Analysis and Results **53**
4.1. Silicon sensor analysis . . . 53
4.1.1. Noise and pedestal analysis . . . 53
4.1.2. Gain . . . 54
4.1.3. Cluster analysis . . . 55
4.1.4. Beam profiles . . . 56
4.1.5. Signal histograms . . . 58
4.2. Energy correction of MedAustron data . . . 60
4.3. Stopping power determination . . . 62
4.4. Sensor current at high rate proton beam . . . 64

5. Conclusions and Suggestions **65**

Bibliography **67**

Glossary **71**

A. Appendix **72**
A.1. Software used for this thesis . . . 72
A.2. Important hints for the usage of the ALiBaVa system . . . 72
A.3. Work input . . . 72

1. Introduction and Background

1.1. Motivation

As Bertold Brecht insinuates, Galileo Galilei once said *"The aim of science is not to open the door to infinite wisdom, but to set a limit to infinite error."*[a]. Independent from its historical validation, this quotation is true in many ways: An important part of science is to limit data error. For example, in particle physics experiments like CMS at the LHC (Chtapter 1.2 and 1.3), improved precision of measurements can be achieved by increasing the collision rate to generate more events in reasonable time, in order to improve statistical significance. The number of collisions per time and bunch overlap area is defined as luminosity:

$$L \ (\mathrm{cm^{-2}s^{-1}}) = \frac{f\ n\ N_1\ N_2}{A} = \frac{f\ n\ N_1\ N_2}{4\pi\sigma_x\sigma_y} \tag{1.1}$$

where f is the revolution frequency, n the number of particle bunches in the storage ring, N_1 and N_2 the number of particles per bunch and A the area of bunch overlap.
It is aside from collision energy (which sets an upper limit for the capability of producing new particles), the most important parameter of a storage ring. Usually the beam profile follows a Gaussian distribution with $\sigma_{x,y}$. To determine the number of produced particles N with a reaction cross section σ over the lifetime T of an experiment, the integrated luminosity L_{int} is used:

$$N = \sigma L_{\mathrm{int}} = \sigma \int_0^T L\, dt \tag{1.2}$$

Since the main goal of colliding beam experiments is to produce particles (in large part at high energies), the detector elements are located in a harsh radiation environment. As one can guess, particle flux increases linear with luminosity, so higher integrated luminosities lead to elevated radiation doses for the surrounding material.
A way to increase spatial resolution is downsizing detector elements, to reduce error margins for tracking and vertexing. However, reducing the detector size leads to new challenges such as stricter requirements for readout electronics and cooling.
By implication, both approaches (increasing spatial resolution and luminosity) are common strategies to improve modern high energy experiments. Not only the detector layout have to be improved, but also its material properties. Consequently, future accelerators such as the HL-LHC (see Chapter 1.2) and it's experiments need preparatory research for new materials and detector structures.

[a] Brecht, *Life of Galileo* (1939)

1.2. LHC - Large Hadron Collider

The Large Hadron Collider is currently (2018) the largest storage ring, featuring the highest particle energy (6.5 TeV per beam, CERN[1] 2017/07), the largest machine and the most complex scientific structure to date. It was constructed and is administered by the European Organization for Nuclear Research (CERN, Organisation européenne pour la recherche nucléaire).
The achievable collision energy of a proton storage ring is mainly determined by circumference r and magnetic field of the dipole magnets B. Now, for the particle's momentum p, one gets:

$$p = q \cdot r \cdot B \quad \longrightarrow \quad p\left[\frac{\mathrm{GeV}}{\mathrm{c}}\right] = 0.3 \cdot r[\mathrm{m}] \cdot B[\mathrm{T}] \tag{1.3}$$

At energies in the TeV scale, rest mass of protons ($\approx$1 GeV/c^2) becomes negligible, hence $E \approx p \cdot c$.

circumference	26 659 m
nominal energy	6.5 TeV (protons), 2.76 TeV/nucleon (ions)
luminosity	10^{34} cm^{-2}s^{-1}
bunches/beam	2 808 (protons)
protons/bunch	$1.15{\cdot}10^{11}$
bunch spacing	25 ns
average/peak bunch crossing rate	31.6 MHz / 40 MHz
average collisions per crossing	20
stored beam energy	360 MJ
circulating current/beam	540 mA
peak dipole field	8.33 T

Table 1.1.: Parameters of the Large Hadron Collider (CERN[1], 2018/03)

Furthermore, energy loss by bremsstrahlung (see Chapter 2.1.2) is inverse proportional to the square of the particle's mass, so the proton (1836 times the mass of an electron) is favored for high collision energies in storage rings. However, proton collisions[b] produce many unwanted secondary effects, so electrons as elementary particles are still useful for experiments, especially in linear accelerators such as the future International Linear Collider (ILC [2]) where bremsstrahlung is not a main limiting factor.

High-Luminosity LHC

For the LHC, an increase in luminosity by a factor of 10, up to 10^{35} cm^{-2}s^{-1} is planned to be accomplished in 2026. Enhanced luminosity means higher particle flux, which leads to increased radiation doses applied to the detectors, as well as higher data rates. To meet these new issues, the accelerator infrastructure and the detectors have to be successively upgraded. Figure 1.2 illustrates the current (2018) time schedule for the accelerator's

[b] protons are compounds of quarks and gluons

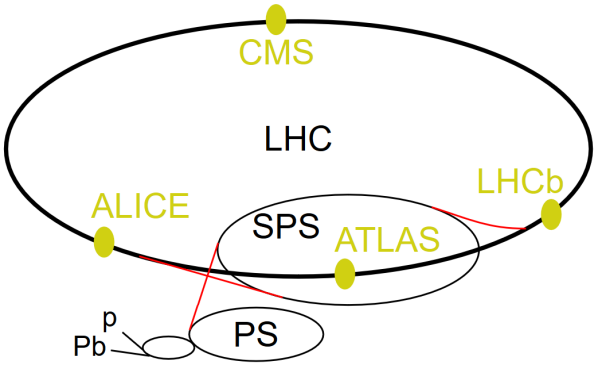

Figure 1.1.: Accelerators and interaction points of the Large Hadron Collider (CERN[1], 2018/01)

runs and shutdowns for upgrading the experiments. The planned luminosity as well as the integrated luminosity is also represented.

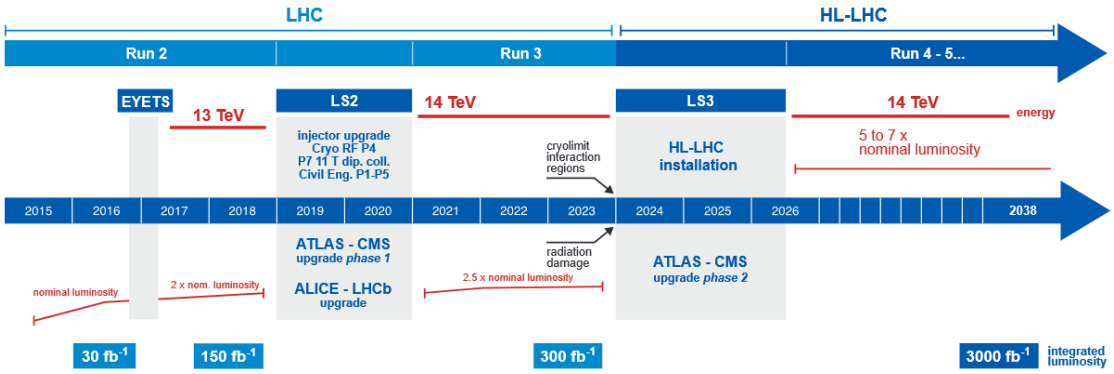

Figure 1.2.: Run and shutdown schedule of the LHC for the next decade (CERN[3], 2018/03)

The LHC's four main experiments (see Figure 1.1)

- ALICE - A Large Ion Collider Experiment
- ATLAS - A Toroidal LHC Apparatus
- CMS - Compact Muon Solenoid
- LHCb - LHC-beauty

aim at testing the predictions of modern particle physics theories, like the Brout-Englert-Higgs mechanism, furthermore physics beyond Standard Model at energy ranges in the TeV scale, for example search for dark matter, Supersymmetry, (SUSY), extra dimensions, but also aspects of heavy ion collisions and precision measurements of known particles.

1.3. CMS experiment

At LHC, CMS (located at Cessy in France) is the largest experiment in terms of mass. It is designed as a general purpose detector, containing different types of detectors, arranged in interlaced layers, each specialized to a certain particle type (CMS:2008[4], page 1ff).
The characteristics of the CMS experiment can be summarized as follows:

- General purpose detector
- Capability of muon identification and measurement of momentum
- For charged particles in general: High momentum resolution and spatial track resolution in the Inner Tracker
- Good energy resolution for charged elementary and composed particles like mesons and hadrons

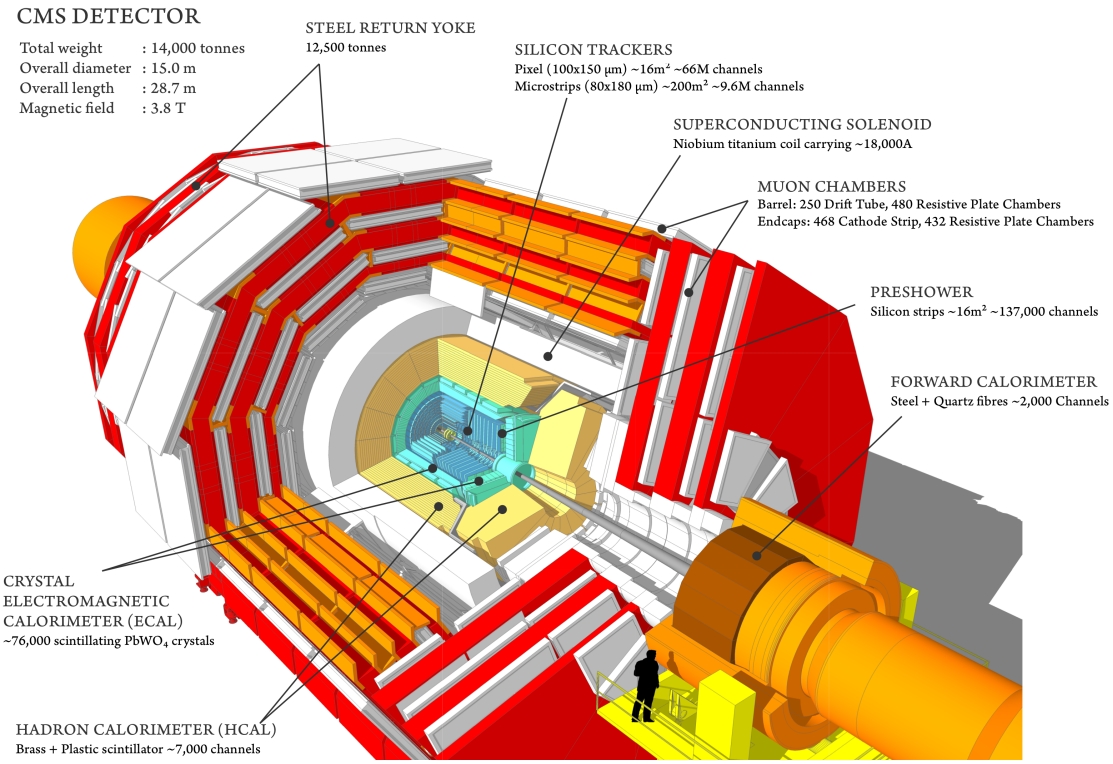

Figure 1.3.: Schematic view of the components of the CMS detector (CERN[1], 2017/07)

1.3.1. Subsystems

Figure 1.3 shows a schematic view of the physical CMS structure. Since sensor types in high energy physics experiments are sensitive to certain particle properties, CMS has a shell structure of detector components sensitive to different particle types. Figure 1.4 illustrates the particle sensitivity of the different detector elements.

One of the essential components is the solenoid magnet which gives CMS its name. It

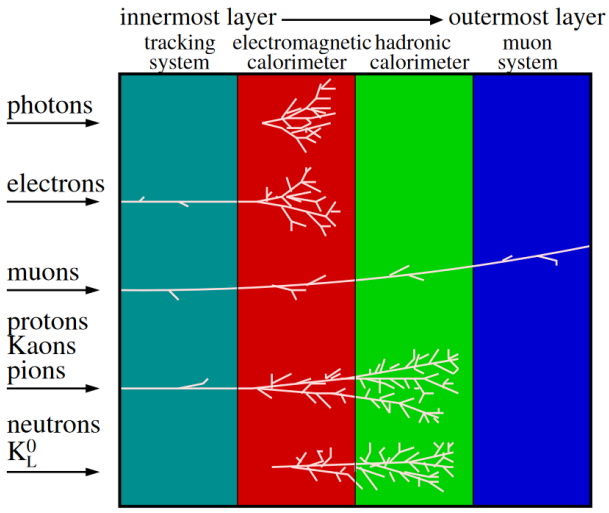

Figure 1.4.: Particle signatures in CMS (Lippmann 2012[5])

consists of a cylindrical superconducting coil and generates a magnetic field of 3.8 T at 18 kA. The field is confined to the detector volume by a steel return yoke.

For determining momentum of charged particles, one way is to track the deflection in this magnetic field, which is described by the Lorentz force (non-relativistic):

$$\vec{F} = q\,(\vec{E} + \vec{v} \times \vec{B}) \tag{1.4}$$

where q is the charge of the particle, $\vec{E}$ and $\vec{B}$ the electric and magnetic fields and $\vec{v}$ the speed of the particle.

When setting $\vec{E} = 0$ (in a tracking system, there is usually no external electric field) and $\vec{v} \perp \vec{B}$ (considering the transversal components in the cylinder geometry) this equation reduces to:

$$F = q\,v\,B \tag{1.5}$$

Identified by the centripetal force $F = m\,v^2/r$ and momentum $p = m\,v$, one gets

$$p = q\,r\,B \tag{1.6}$$

where r is the radius of the circular particle trajectory.

Through B is known because it is applied externally, the challenge is to determine r as precise as possible (tracking). It stands to reason that the spatial resolution of the tracker is therefore directly linked to the precision of the momentum measurement.

Inner pixel system

The density of produced particles is higher at inner layers, arising from their radial trajectories originating at the collision point. For vertexing, this circumstance requires the highest spatial resolution at the nearest entry point into the detector to achieve highest precision. Therefore, at this location a pixel sensor with high granularity is used, leading to high spatial resolution.
Both, tracking and vertexing, demand the lowest material budget possible, in other words the material deployed has to be minimized. This is caused by the interaction of particles with matter which causes deflection through scattering, leading to loss in track and vertex resolution.

The interaction point of CMS is surrounded by a new (installed 2017) Inner Tracker

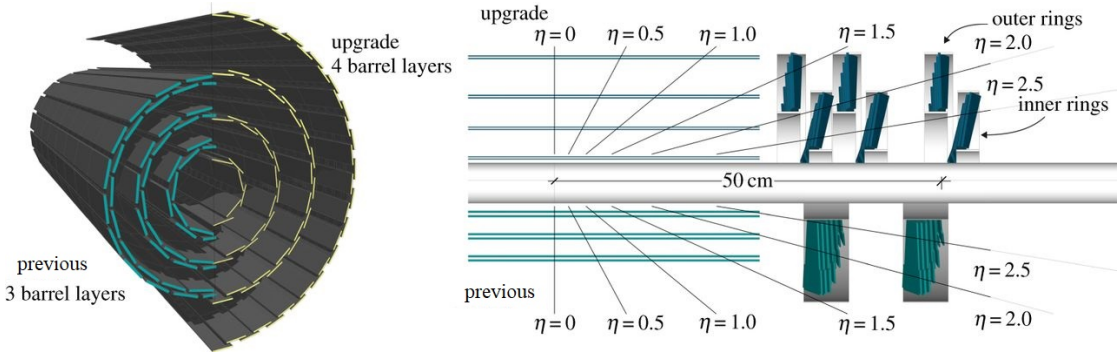

Figure 1.5.: Inner pixel system since Phase-I Upgrade, compared to the predecessor (Wells 2014[6])

which consists of 1184 silicon pixel sensor modules, arranged in four barrel layers. Phase-I Upgrade (Figure 1.2) of the inner system has already been executed. Figure 1.5 illustrates the actual layout, compared to its predecessor. The three endcap layers for each side consist of 672 pixel modules in total. In total, 124 million pixels are installed in the Inner Tracker (CERN-Phase1-CMS-Pixel[7], page 59ff). Its location nearest to the interaction point in the beam line leads to the highest radiation doses. Through its high granularity, a CO_2 cooling system with a capacity of 15 kW is installed to relieve the heat load and allowing temperatures down to -20°C without water condensation. (CERN-CMS1-Pixel[7], page 161).

Outer tracking system

Adjacent to the inner pixel tracker, the outer silicon strip tracker consists of 24 244 detector modules in four subsystems, each of them encased by a carbon fiber or graphite frame. The active sensor area of each module varies between 6 243 mm^2 and 17 202 mm^2, depending on the module's location (CMS 2008[4], page 55ff). Each module has 512 or 768 strips, read out by 256 channels. The total number of sensor strips is 9.3 million, making up a total active area of 198 m^2. Compared to the Inner Tracker, the silicon strip

sensors have a reduced spatial resolution and less readout channels, therefore a lower granularity. This may be seen as a disadvantage, however, it leads to lower demands regarding readout electronics, less complex power supply, and therefore less power dissipation. Furthermore, the density of particle tracks decreases with increasing distance to the collision point, which lowers the need for granularity in Outer Tracker regions.
The Outer Tracker geometry is built up of 12 layers in the barrel and 10 layers per end cap. The front-end electronics consists of 128 channel readout chips, whose pipeline is 192 elements deep. The sampled signals undergo preamplification and pulse shaping via an APV25 (Friedl 2011[8]) front-end amplifier, at a frequency of 40 MHz, which matches the bunch crossing frequency (see Table 1.1)

Electromagnetic Calorimeter

The purpose of the Electromagnetic Calorimeter (ECAL) is the measurement of particle energies. It is only able to detect particles interacting via the electromagnetic force. Energy deposition is determined via scintillation (see Chapter 2.2) of lead tungstate ($PbWO_4$) crystals, which are highly dense ($8.28\,g/cm^3$) but optically clear. The detector characteristic is linear, what means that produced scintillation light is proportional to the deposited particle energy. The yield of this material is comparably low (4.5 photoelectrons per MeV), which requires efficient photodetectors (CMS 2008[4], page 90).
For the barrel, these goals are met by avalanche photodiodes, at a gain of 50 and an active area of $5{\cdot}5\,mm^2$ for each diode. The quantum efficiency is 75 %. A pair of diodes is mounted on each crystal. The crystals are set in a matrix of carbon fibre to keep them optically isolated.
In the endcaps, the lower magnetic field enables the use of vacuum phototriodes. Each phototriode has an active area of $280\,mm^2$, one sensor is mounted on each crystal. The phototriodes have a quantum efficiency of 22 % and a gain of ≈10 (CMS 2008[4], page 90ff).

Hadron Calorimeter

For the measurement of high energy hadronic particle jets (induced by the strong interaction), the Electromagnetic Calorimeter is surrounded by the Hadron Calorimeter (HCAL). For measuring hadronic energy deposition, it is set up in a sandwich structure (sampling calorimeter), where layers of dense material (brass and steel) alternate to layers of plastic scintillators.
The active medium consists of 70.000 tiles of scintillating fibers with wavelength shifting; light is guided to hybrid photodiodes (photomultiplier tubes for amplification and avalanche diodes for detection of PMT electrons, gain ≈2000). (CMS 2008[4], page 122ff)

Muon system

As the name "Compact Muon Solenoid" suggests, detecting muons is one of the most important tasks of the CMS experiment. As one of the most distinguishable decay

channels of the Higgs boson is $H \rightarrow ZZ^{(*)} \rightarrow 4l$, whereas Z is the Z boson and l are leptons (CMS 2012[9]), muons provide an interesting particle signature. Because muons are more penetrating than most other particles, the muon system is the outermost layer, installed in the return yoke.
The magnetic field (2 T) in the muon system is antiparallel to the field of the inner layers (3.8 T), leading to a typical S-curve signature of muons. The principle of momentum determination is identical to the tracker of the inner layers, by measuring the curvature of trajectory. For tracking the muons, the system consists of two types of detectors: drift tubes in the central barrel and cathode strip chambers in the end caps. For triggering, resistive plate chambers are installed at both locations.(CMS 2008[4], page 162ff)

1.3.2. Phase-II Upgrade

As mentioned in Chapter 1.2, the detectors of the experiments have to be upgraded to meet the requirements of the HL-LHC. Through elevated collision rates and higher track densities, the required spatial resolution as well as the resulting data rate increases over few orders of magnitude (CERN-LHCC: Phase II[10], page 25ff). Higher collision rates also increase the particle flux, so radiation hardness must be improved to meet the HL-LHC requirements. During the life cycle, HL-LHC is planned to reach an integrated luminosity of 3000 fb^{-1}, 10 times compared to the actual run schedule of 300 fb^{-1}, completed in the end of 2023. At this point, the existing sensors will be afflicted by serious radiation damage; many of them already failed. Therefore the present detector elements have to be replaced.
As mentioned in Chapter 1.3.1, the Phase-I Upgrade of the inner pixel detector has already been executed. For the Phase-II Upgrade (Figure 1.2), it is planned to install new strip sensors in the Outer Tracker (Figure 1.6). Prototypes for the upgrade are currently provided by the vendors Infineon and Hamamatsu. Infineon[c] is an interesting candidate because of its geographical proximity to CERN and HEPHY and long-term experience in semiconductor development and production. P-type sensors are preferred because of their superior radiation hardness. To pass the qualification process, multiple parameters like electrical characteristics, mechanical stability, optical quality and performance under irradiation have to be verified.
In this diploma thesis, four different sensor types (three from Infineon, one from Hamamatsu) were investigated related to electrical properties (see Table 3.1). For testing in particle beam environments, testbeam studies at accelerators (MedAustron in Wiener Neustadt and DESY II in Hamburg) were conducted.

[c] located in Villach, Austria

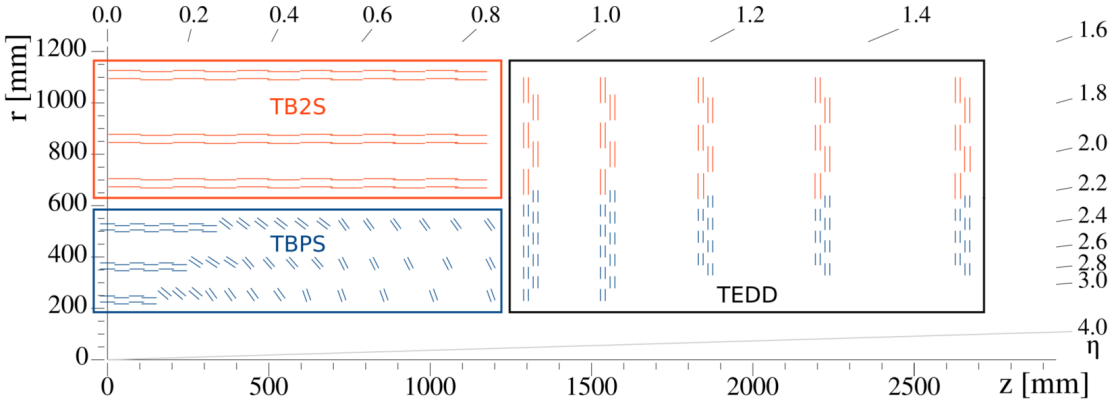

Figure 1.6.: Sketch of the prospective Outer Tracker layout of Phase-II. TB2S = Tracker Barrel with 2S modules, TBPS = TB with PS modules, TEDD = Tracker Endcap Double-Discs (CERN-CMS2-Tracker[11], page 27)

1.4. MedAustron

MedAustron is a proton and heavy ion[d] synchrotron used for proton and heavy ion therapy, medical, biological and high energy physics experiments. Its circumference is 78 m with 16 dipole and 24 quadrupole magnets. At the testbeams, maximum proton beam energy was limited to 252.7 MeV, but 800 MeV should be available through 2018. In order to test the performance of strip sensor prototypes, two testbeams in night shifts (further denoted by "TB 1" and "TB 2") at MedAustron were conducted at irradiation line 1 (see Figure 1.7).

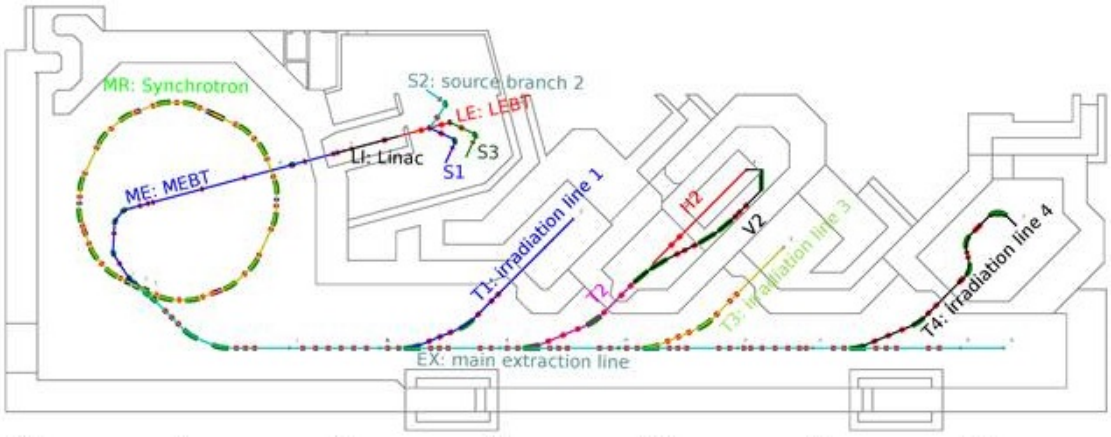

Figure 1.7.: Layout of the MedAustron accelerator (CERN[1], 2017/12)

[d] C^{6+} not yet available, should be commissioned during 2018, He^{2+} maybe in the near future

circumference	78 m
energy range	62.4-800 MeV* (p^+), 120-400 MeV/u (C^{6+})
beam size (FWHM)	4 mm
number of bunches	1
maximum particles/spill	$2 \cdot 10^{10}$
maximum intensity	$3 \cdot 10^{10}$/s (p^+), $4 \cdot 10^8$/s (C^{6+})
revolution frequency for p^+	1.3 MHz (62.4 MeV) to 2.5 MHz (252.7 MeV)
revolution frequency for ions	470 kHz (7 MeV/u)
maximum beam current	8 mA
nominal extraction time	5 s
minimum irradiation time	1 ms
dipole magnets	16
quadrupole magnets	24
number of RF cavities	1

Table 1.2.: Beam parameters of the MedAustron synchrotron (Schreiner 2018[12]) *800 MeV were not available at the testbeams, but should be available through 2018

1.5. DESY - Deutsches Elektronen-Synchrotron

DESY is named after its first accelerator (DESY I, first operation in 1964), an electron synchrotron with a beam energy of 7.4 GeV. At this time, it was the largest device of its type. 1966, quantum electrodynamics was confirmed by this accelerator. DESY II was taken into operation in 1987, was used as pre-accelerator for DORIS and PETRA and was the source for the electron testbeam in this thesis (See Figure 1.9). Later, DESY I was upgraded to DESY III (1988), which served as a proton synchrotron (and injector for PETRA) until 2007.

DORIS (Doppel-Ring-Speicher, "double-ring storage") was DESY's second circular accelerator and its first storage ring with a circumference of 300 m. This synchrotron conducted for electron-positron collisions up to 5 GeV per beam and was shut down 2012 in favor of its successor PETRA III.

PETRA (Positron-Elektron-Tandem-Ring-Anlage, "positron-electron tandem-ring facility") was finished in 1978. One of its biggest successes was the discovery of the gluon 1979. It is an electron-positron collider with a circumference of 2304 and an energy of 19 GeV per beam.

HERA (Hadron-Elektron-Ring-Anlage, "Hadron-Electron Ring Facility") was DESY's largest collider, with a circumference of 6336 m. It was the world's first collider using primarily superconducting magnets. Electron energies were at 27.5 GeV, proton energies at 920 GeV. It was shut down in 2007.

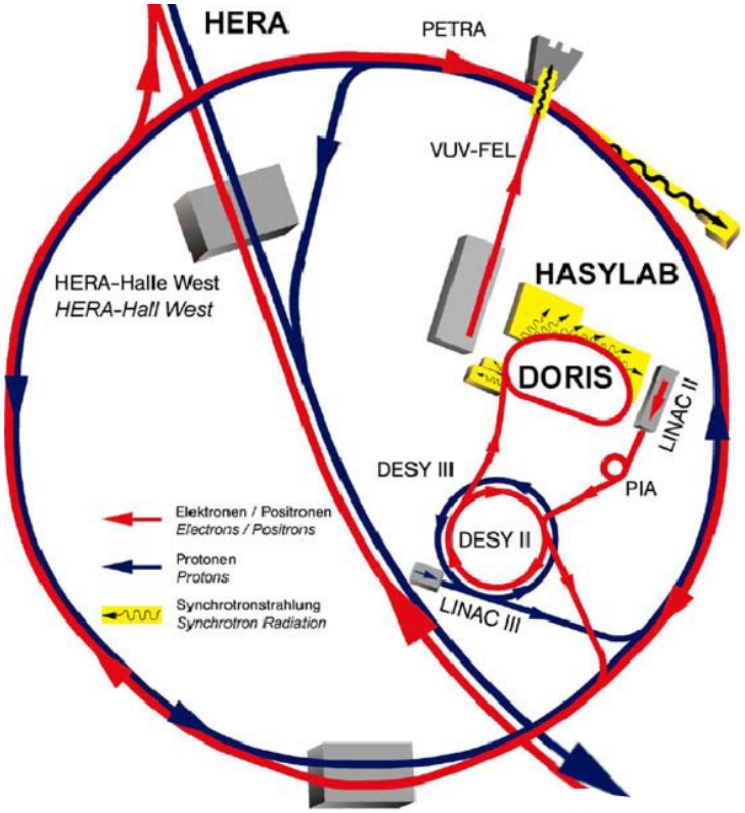

Figure 1.8.: Accelerators at DESY

circumference	292.8 m
ejection energy	4.5 GeV (DORIS), 6.0 GeV (PETRA)
bunches/beam	1
electrons/bunch	up to $3{\cdot}10^{10}$
bunch length (FWHM)	23 mm
number of cavities	8
max. cavity voltage	13.5 MV
cavity radio frequency	499 MHz
max E loss per revolution	7.83 MeV
E precision (ΔE/E)	$1.2{\cdot}10^{-3}$

Table 1.3.: Parameters of the DESY II synchrotron (DESY II[13], 2018/02)

Electron beam generation at DESY II testbeam sites

At the testbeam sites at DESY II, the electron beam is not directly extracted, because this would have an unacceptable influence to the electrons injected to other experiments (see Chapter 1.5).

Instead, a carbon fiber target is placed in the circulating beam of the synchrotron (see

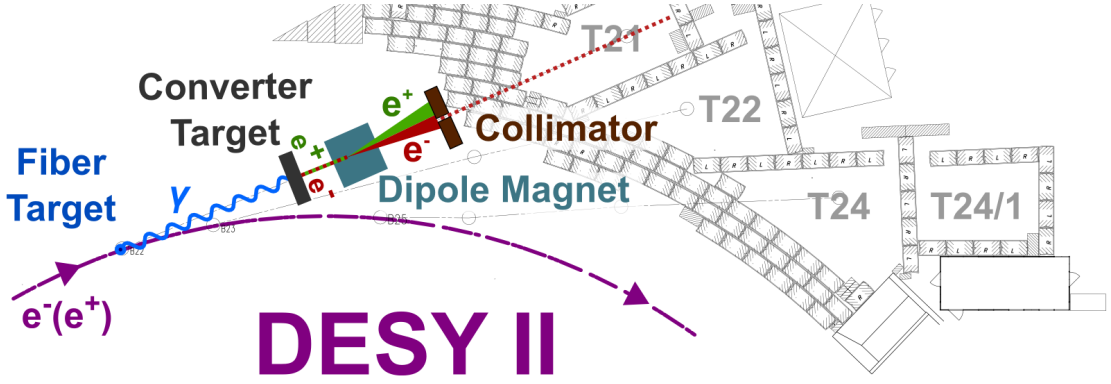

Figure 1.9.: DESY II synchrotron with test beam sites and electron/positron extraction (DESY II[13], 2017/12)

Figure 1.9). This produces bremsstrahlung which is converted to electron/positron pairs by a metal plate (converter, Cu or Al). A dipole magnet is used to spread out the forward electron/positron beam spectrum. Via a collimator, only a small slice of the incident beam is cut out of this spectrum. As deflection of charged particles in a magnetic field depends on particle energy and magnetic field (see Equation 1.4), the testbeam user is able to choose electron/positron energy by variation of the dipole magnet coil current (DESY II[13], 2017/12).

2. Theory of Particle Detectors

2.1. Interaction of charged particles with matter

2.1.1. Excitation of electrons: Scintillation

A high energy particle hitting matter can transfer a part of its kinetic energy via inelastic collisions. This may lead to electronic excitation and relaxation. Another process is ionization, followed by recombination. If these relaxation processes emit photons (usually in the visible or UV spectrum), they are referred to as "scintillation". In an ideal scintillator, the radiated light is proportional to the transferred particle energy:

$$Y(\lambda) = \frac{\langle N(\lambda) \rangle}{E} \tag{2.1}$$

where $Y(\lambda)$ is the light yield, $N(\lambda)$ the number of photons at a specific wavelength and E the deposited energy (Kolanoski 2015[14], page 496).
For scintillation, it is important that the emission wavelength is longer than the absorption wavelength (Stokes shift), otherwise the emitted photons would be re-absorbed by the medium itself. A Stokes shift requires at least two available energy transitions, where the relaxation of one intermediate state is non-radiative (vibrational or heat dissipative).

2.1.2. Bremsstrahlung

When charged particles enter matter, they unavoidably interact with the Coulomb fields of nuclei (dominant) and other electrons (see Figure 2.1). Assuming no momentum is transferred to a nucleus (fixed target, justified by its high mass) and force is defined by the change of momentum, the non-relativistic Coulomb force acting on an electron can be written as:

$$\vec{F} = \frac{d\vec{p}}{dt} = \frac{q\,Q}{4\pi\epsilon_0 \|r\|^3}\vec{r} \tag{2.2}$$

whereas the point of origin is at the position of the nucleus, $q = e$ is the charge of the electron, $Q = Z\,e$ is the charge of the nucleus, $\vec{r}$ is the distance electron-nucleus and ϵ_0 is the vacuum permittivity (electric constant).
Since the electron loses energy and momentum, conservation of momentum and energy requires a photon to be emitted; its energy is given by $h \cdot f = E_1 - E_2$. These emitted photons are the bremsstrahlung. Bremsstrahlung typically has a continuous spectrum (exception: bremsstrahlung created by undulators in free-electron lasers), which becomes more intense and whose peak intensity shifts toward higher frequencies as the change of

[a] https://en.wikipedia.org/wiki/Bremsstrahlung, 2018/03

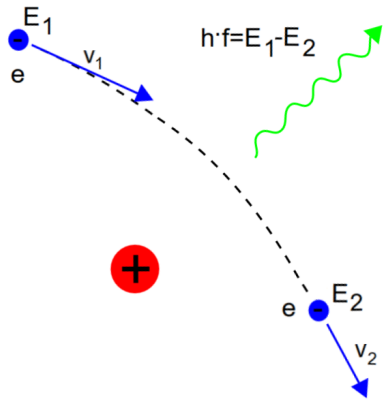

Figure 2.1.: Bremsstrahlung radiated from an electron in the Coulomb field of a nucleus[a]

energy of decelerated particles increases.
The mean energy loss per path length through bremsstrahlung is approximated by:

$$-\left.\frac{dE}{dx}\right|_{\text{rad}} \approx 4\alpha\rho N_A \frac{Z(Z+1)}{A} z^2 \left(\frac{1}{4\pi\epsilon_0}\frac{e^2}{mc^2}\right)^2 E \cdot \ln(183 \cdot Z^{-1/3}) \tag{2.3}$$

whereas $\alpha \approx 1/137$ is the fine structure constant, ρ is the mass density of the target material, N_A is the Avogadro constant, Z the target's atomic number, A its mass number, z the charge number of the projectile (1 for electrons), m its mass and E its energy.
As Equation 2.3 shows, the radiative contribution is linear to energy, but inverse proportional to the square of the projectile's mass. The proton's mass is about 1836 times higher than the mass of an electron, therefore the radiative losses of electrons are 3.4 millions higher, so it is the dominant energy loss mechanism for particle energies more than 100 MeV (see Figure 2.2). In contrast to electrons, the energy loss of protons at energies in the MeV range is dominated by inelastic collisions (see Figure 2.3), so bremsstrahlung is negligible. However, at energies in the GeV scale, the contribution of radiative energy loss becomes dominant.

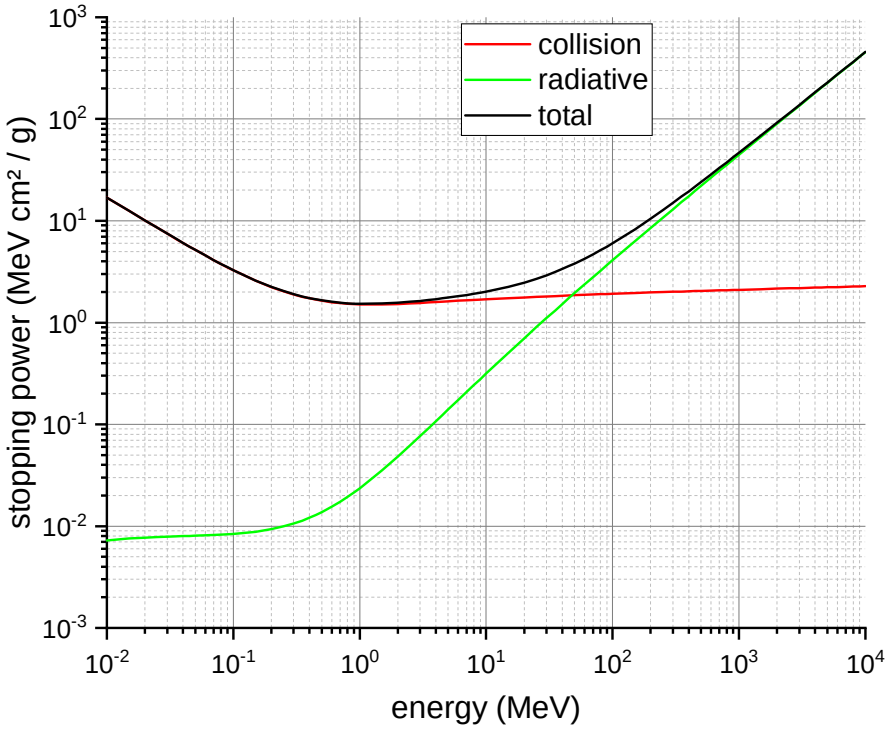

Figure 2.2.: Mass stopping power for electrons in silicon as a function of the energy of the incident particle (NIST ESTAR[15], 2018/03)

2.1.3. Ionizing effects

Bethe-Bloch equation

The Bethe-Bloch formula describes electronic energy loss by the incident of massive particles[b]. It is derived from inelastic projectile-electron collisions, using the premise that incident particle energies $\gg$ electron binding energies, so detector electrons can be seen as resting in the lab frame of reference.
After few derivation steps, the differential mean energy loss per path length (or stopping power) is now given by:

$$-\left.\frac{dE}{dx}\right|_{\text{coll}} = Kz^2\frac{Z}{A}\frac{1}{\beta^2}\left[\underbrace{\frac{1}{2}\ln\frac{2m_e c^2\beta^2\gamma^2 T_{\max}}{I^2}}_{\text{semi-relativistic}}\underbrace{-\beta^2}_{\text{relativistic correction}}\underbrace{-\frac{\delta(\beta\gamma)}{2}}_{\text{density correction}}\right] \tag{2.4}$$

[b] except electrons because they are not distinguishable by means of quantum mechanics

where $\beta = \frac{v}{c}$ and $\gamma = \frac{1}{\sqrt{1-\beta^2}}$.

symbol	**name**	**value/unit**
$m_e c^2$	electron mass $\cdot$ c^2	0.510998918(44) MeV
r_e	classical electron radius $e^2/4\epsilon_0 m_e c^2$	2.817940325(28) fm
N_A	Avogadro constant	$6.0221415(10)\cdot 10^{23}$ mol^{-1}
K	$4\pi N_A {r_e}^2 m_e c^2$	0.307075 MeV g^{-1} cm^{-2}
T_{max}	maximum transferred kinetic energy	eV *(nota bene!)*
z	charge of incident particle $n \cdot e$	
Z	atomic number of absorber	
A	atomic mass of absorber	g mol^{-1}
I	mean excitation energy	eV *(nota bene!)*
$\delta(\beta\gamma)$	density effect correction	

Table 2.1.: Parameters of the Bethe-Bloch equation in high energy physics units (PDG 2007[16])

It should be noted that the stopping power using this formula is highly dependent on the mass density of the target material. Especially for comparing diverse materials which can be in different aggregate states, it is more useful to divide the stopping power by the mass density to get the mass stopping power, which now is nearly independent of target mass density (see Figure 2.3). The Bethe-Bloch formula provides a good description for energy losses in the momentum range of $0.1 < \beta\gamma < 100$. At lower momentums the premise of short interaction time (equivalent to electrons at fixed positions) is not valid any more, whereas at higher energies radiative effects increase which are not covered by the Bethe-Bloch model.
The mean range Δx of a particle can be approximated by integrating the reciprocal linear stopping power 1/S(E) over the continuous energy loss (continuous slowing down approximation CSDA):

$$S(E) = \frac{dE}{dx} \tag{2.5}$$

$$\Delta x = \int_0^{\Delta x} dx = \int_0^L \frac{dE}{dE} dx = \int_0^{E_0} \frac{dx}{dE} dE = \int_0^{E_0} \frac{1}{S(E)} dE \tag{2.6}$$

where E_0...initial kinetic energy of the incident particle. The fluctuations of Δx are usually small.
In contrast to electrons and photons, hadrons have low stopping power at high energies in the upper MeV range (≈ 0.7 keV/µm at 100 MeV) and high stopping power (≈ 30 keV/µm at 1 MeV) in the lower MeV range (see Figure 2.3), where the $1/\beta^2$ term of the Bethe-Bloch formula is dominating. In a thick absorber, this leads to the conclusion that energy loss is low close to the entry point and is steadily increasing with penetration depth until it reaches a maximum immediately before the particles come to rest (recombination and nuclear reactions). This peak is called the "Bragg peak" (see Figure 2.4). The Bragg

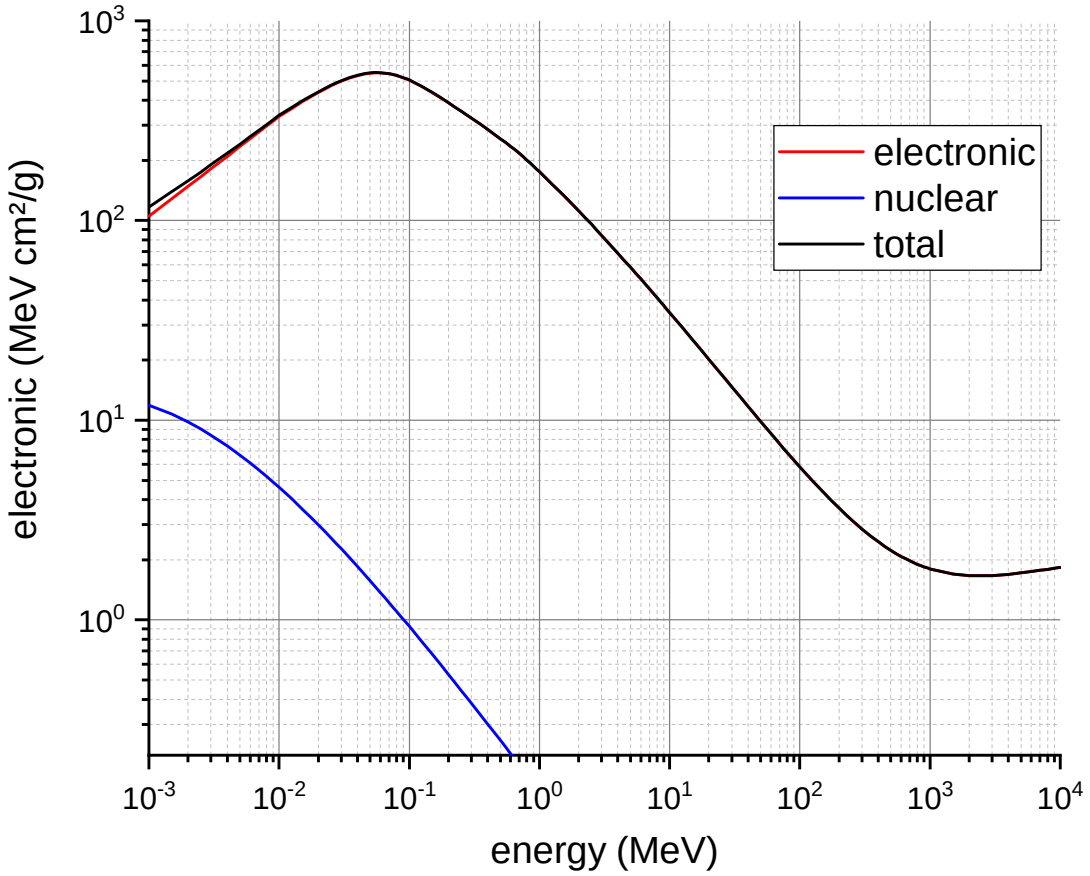

Figure 2.3.: Mass stopping power for protons in silicon as a function of the energy of the incident particle(NIST PSTAR[15], 2018/02)

peak is only relevant for heavy particles, where absorption and elastic scattering can be neglected. The lower part of the right flank is dominated by absorption of protons by nuclear reactions (Kolanoski 2016[14], page 53ff).

Since deposited energy by inelastic scattering is linked to deposited radiation dose and the depth of the Bragg peak is dependent on particle energy, the potential is given to control the energy deposition depth of hadrons. As one can imagine, this opens huge possibilities in radiation therapy over conventional treatments with photons and electrons, because applied doses can be focused to the target tissue while sparing the surrounding healthy organs. Application and research of hadron therapy is the main operational purpose of the MedAustron (Chapter 1.4).

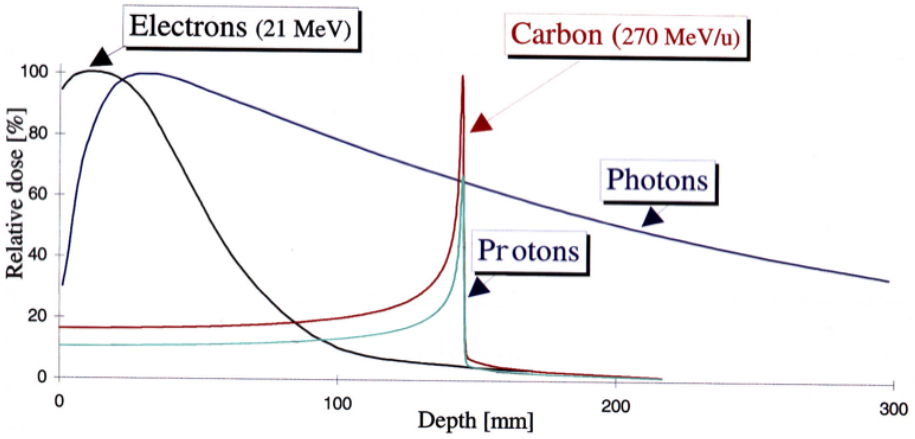

Figure 2.4.: Relative dose distribution for different particles in water (QD[17], 2018/03)

δ-electrons: High energy transfer knock-on

During the passage of massive charged particles through matter, most collisions are characterized by comparably small energy transfers $T \ll E_{inc}$, whereas E_{inc} is the kinetic energy of the incident particle. δ-electrons are defined as released electrons having enough kinetic energy to ionize several other atoms, thus causing a track of secondary ionizations. Figure 2.5 illustrates that most δ-electrons are emitted through near-central collisions, where the energy transfer is higher.

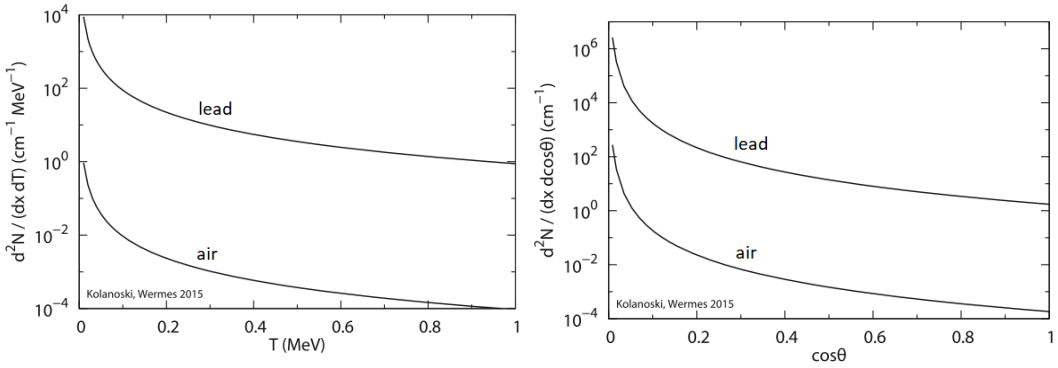

Figure 2.5.: Energy (left) and angular (right) distribution of δ-electron emission for protons as projectiles. This is an approximation for resting shell electrons and high energy transfer, so not any more valid at $\cos\theta \approx 0$ (Kolanoski 2016[14])

2.1.4. Gaussian distribution

For thick detectors (thickness $\approxeq$ particle range), the deposited energy profile follows a Gaussian distribution. The probability density function (PDF) is:

$$p(x) = \frac{1}{\sigma\sqrt{2\pi}} \exp\left(-\frac{(x-\mu)^2}{2\sigma^2}\right) \tag{2.7}$$

where σ...standard deviation and μ...mean.
For a pure Gaussian distribution, the most probable value (MPV, peak) is equal to the mean value. Figure 2.6 shows a Geant4 simulation of the energy deposition of low energy antiprotons in silicon.

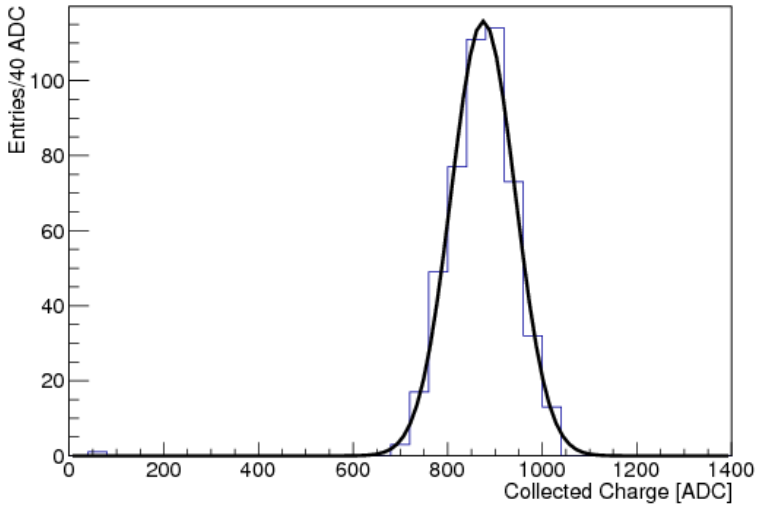

Figure 2.6.: Geant4 simulation of the energy deposition of low energy antiprotons in silicon[c]

2.1.5. Landau distribution

For thin detectors (thickness $\ll$ particle range), the deposited energy profile follows a Landau distribution. The PDF is:

$$f(\lambda) = \frac{1}{2\pi i}\int_{c-i\infty}^{c+i\infty} \exp(s\ln s + \lambda s)ds = \frac{1}{\pi}\int_0^\infty \exp(-t\ln t - \lambda t)\sin(\pi t)dt \tag{2.8}$$

where s is a scale parameter ($s \in \mathbb{R}^+$).

Figure 2.7 shows a Landau distribution. Its asymmetry is apparent, so the most probable value ($\lambda_{MPV} = -0.22278$) is different from the mean value. The long tail is caused by high energy secondary electrons (δ-electrons, see Chapter 2.1.3), whose energy gain is higher than the average. The main part of these secondary electrons will leave the

[c] http://inspirehep.net/record/1265279/, 2018/02

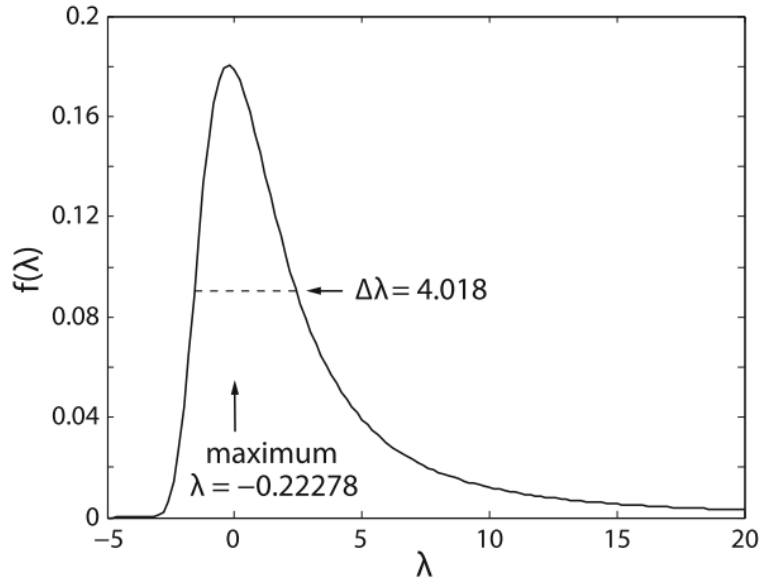

Figure 2.7.: Probability density function of a Landau distribution (Kolanoski 2016[14])

detector plane after a few µm, but some will have a trajectory nearly parallel to it, causing many secondary ionizations and therefore a high energy deposition.
Like the Gaussian distribution, the Landau distribution has to be transformed for description of energy losses. In real detectors, the measured distribution is always a convolution of a Landau and at least one Gauss PDF, where the additional Gauss PDFs originate from uncertainties of the measurement system.

2.1.6. Vavilov distribution

For discrimination between thick and thin detectors Vavilov (Kolanoski 2016[14], page 47) introduced a parameter κ:

$$\kappa = \frac{\xi}{T_{\max}} \tag{2.9}$$

where ξ is the prefactor of the Bethe-Bloch equation (2.4) times the mean range Δx (equation 2.6):

$$\xi = \frac{1}{2} K \frac{Z}{A} \rho \frac{z^2}{\beta^2} \Delta x \tag{2.10}$$

Now κ determines which distribution is an adequate approximation:

$$\kappa \approx 1 \rightarrow \text{PDF symmetric, Gauss distribution, thick detector}$$
$$\kappa \lesssim 0.01 \rightarrow \text{PDF asymmetric, Landau distribution, thin detector}$$

For a κ between those values, one has to do a Gauss-Landau convolution or use the Vavilov distribution (Kolanoski 2016[14], page 49):

$$p(\lambda; \kappa, \beta^2) = \frac{1}{2\pi i} \int_{c-i\infty}^{c+i\infty} \phi(s) e^{\lambda s} ds \tag{2.11}$$

whereas

$$\phi(s) = e^{C} e^{\psi(s)}, \qquad C = \kappa(1 + \beta^2 \gamma_{\mathrm{E}})$$

$$\psi(s) = s \ln \kappa + (s + \beta^2) \left(\int_0^1 \frac{1 - exp(\frac{-st}{\kappa})}{t} dt - \gamma_{\mathrm{E}} \right) - \kappa \cdot exp(\frac{-s}{\kappa})$$

$$\gamma_{\mathrm{E}} = 0.5772... \quad \text{(Euler-Mascheroni constant)}$$

2.2. Scintillation detector systems

A scintillation detector system typically consists of four elements:

- **Scintillator**: The scintillator creates photons by scintillation (see Chapter 2.1.1).
- **Lightguide**: A lightguide is used for geometrical adaptation from the scintillator to the photosensor. In many applications, the scintillator is cuboid or prismatic, but the photosensor has a circular entry window.
- **Photosensor**: For the detection of the photons, different sensor types are used: Photomultiplier tubes (PMTs), avalanche photodiodes (APDs) and silicon photomultipliers (SiPMs). These types differ in quantum efficiency (10 % to 50 %), gain ($10^{5\text{-}9}$), linearity and rise and dead time (≈10 ps to ns).
- **Electronics**: The purpose of front-end electronics is preamplification, discrimination and shaping of the current pulse. Typically PMTs have a very high gain, so preamplification is not necessary for these detector systems.

The signal chain is illustrated in Figure 2.8

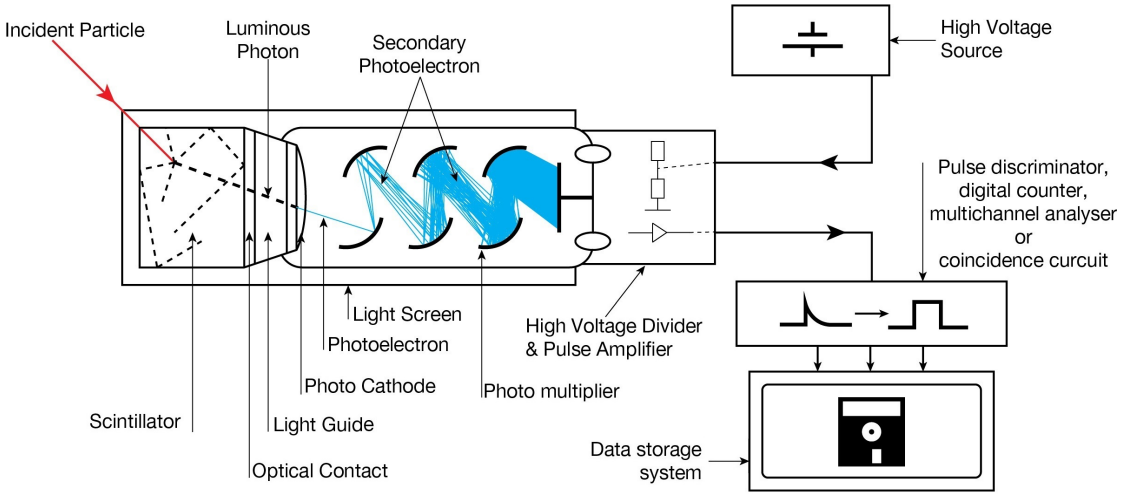

Figure 2.8.: Schematic view on a scintillation detector system[d]

[d] https://en.wikipedia.org/wiki/Scintillation_counter, 2018/03

2.2.1. Scintillators

For high energy physics experiments, many different classes of materials are in use: Organic scintillators (solid and liquid), inorganic crystals, glasses, and polymerized plastic scintillators. Each of these scintillator types has typical properties regarding quantum efficiency, yield, linearity, radiation hardness and time constant. An ideal scintillator should have following characteristics (Kolanoski 2016[14], page 496):

- High quantum efficiency
- Linearity of yield (see Equation 2.1) in terms of deposited energy
- Transparency of scintillation medium
- Short time constant of the relaxation process for fast signal pulses
- Refraction index of scintillation medium close to the lightguide and/or photosensor for efficient optocoupling
- Light collection efficiency as high as possible
- Appropriate atomic number Z, for most cases higher is better, but for neutrons a low Z is favored
- For high-radiation applications, of course radiation hardness is crucial

Wavelength shifters are often used to adapt scintillation wavelength to the optimum of photosensors. These are materials which itself absorb and re-emit photons at larger wavelengths.

2.2.2. Photomultiplier tubes

A photomultiplier tube (PMT, see Figure 2.8) consists of a photocathode, where incoming photons knock out photoelectrons (photoelectric effect). These photoelectrons are accelerated and focused towards a dynode system (secondary electron multiplier) via an electric field. When hitting the first dynode, multiple secondary electrons are emitted and on their part accelerated to the next dynode. This process is repeated for all consecutive dynodes until the secondary electrons are collected at an anode. Through this multi-stage amplification the overall gain of PMTs is very high (10^5 to 10^9) an the resulting signal is directly processible. (Kolanoski 2016[14], page 414ff)

2.2.3. NIM electronics

The Nuclear Instrumentation Module (NIM) standard defines mechanical and electrical specifications for electronic modules and their crates used in particle and nuclear physics. The concept of replaceable modules in crates offers advantages in flexibility, interchange of instruments, reduced design effort, ease in updating and maintaining these instruments. The NIM standard also specifies cabling, connectors, impedances and levels for

logic signals. NIM signals are defined as negative true (at -16 mA into 50 Ω = -0.8 V). Typical NIM modules (as used in MedAustron TB 1) are discriminators. Two general approaches for discriminators are commonly in use:
A leading-edge-discriminator reacts on the rising edge of the signal pulse. It is simple and easy to use, but different rising times (steepness at different pulse heights) lead to uncertainties (time walk) at real-time measurements.
By splitting the signal into two identical signals, inverting and damping one, delaying the other and adding them, a constant fraction discriminator is formed (see Figure 2.9). The combined signal has a zero-crossing, which can be analyzed via a threshold comparator. The resulting trigger signal is now almost independent from input leading edge steepness and pulse height. This technique is more complex than a leading-edge-discriminator, but offers more precision for timestamping or critical real-time applications like time-of-flight measurements (Kolanoski 2016[14], page 740ff).

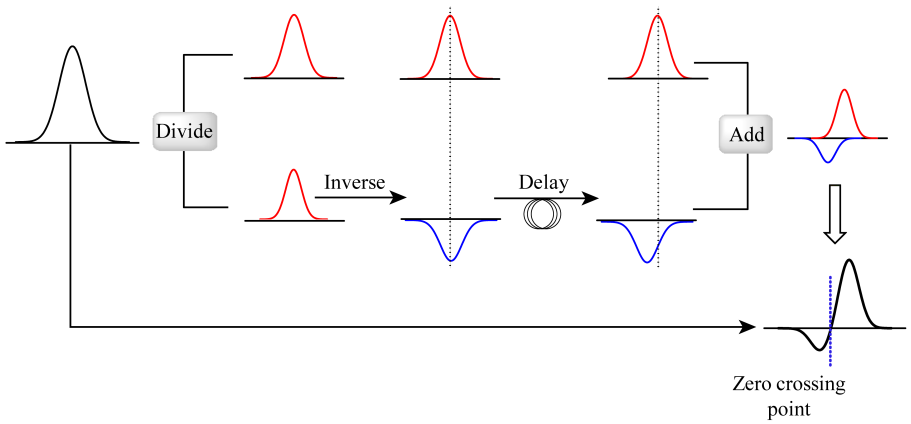

Figure 2.9.: Principle of a constant fraction discriminator[e]

2.3. Semiconductor physics and silicon detectors

In semiconductors, there are two types of charge carriers: Electrons (-e) and holes (+e), whereas their concentration in undoped silicon is about 10^{10} cm^{-3} for each type. Depending on doping type, the concentration[f] differs over many magnitudes of order. The more common charge carriers are denoted by "majority carriers" whereas the lesser common ones are referred to as "minority carriers".
Quantitative description of charge carrier movement in semiconductors is done by the Boltzmann transport equation, similar to the movement in gases. This is possible due to the concept of an "effective mass" (m_{eff}) of the charge carriers, which expresses binding forces to the crystal lattice (Kolanoski 2016[14], page 121 and 122).

[e] https://en.wikipedia.org/wiki/Constant_fraction_discriminator, 2018/03
[f] typically 10^{10}

2.3.1. Drift

An external electric field $\vec{E}$ causes charge carriers to move along the field direction, according to the Drude model (without magnetic fields) (Kolanoski 2016[14], page 122ff):

$$m_{\text{eff}}\dot{\vec{v}} + \frac{m_{\text{eff}}}{\tau}\vec{v_{\text{drift}}} = q\vec{E} \tag{2.12}$$

where

- $\vec{v}$ is the charge carrier velocity
- τ mean time beween collisions (between crystal lattice and valence electrons); time until the next momentum change
- $\vec{v_{\text{drift}}}$ is the charge carrier drift velocity (charge carrier velocity minus thermal velocity)
- $q = \pm e$ is the electric charge of the carrier

In case of constant drift velocity ($\dot{\vec{v}} = 0$), Equation 2.12 reduces to:

$$\vec{v_{\text{drift}}} = \frac{q\tau}{m_{\text{eff}}}\vec{E} = \mu\vec{E} \tag{2.13}$$

whereas μ is identified to the mobility of charge carriers (electrons and holes have to be considered separately).
The Drude model is equivalent to the relaxation time approximation of the Boltzmann transport equation. τ is mainly dependent from temperature, but also from the electric field strength. Figure 2.10 shows that in case of small fields ($E < 10^3\,V/cm$), it is nearly constant, but in typical fields of semiconductor detectors ($E \approx 10^6\,V/cm$) this approximation is not valid any more. This is caused by higher drift velocity v_{drift} with increasing field, but it saturates at fields of $E < 10^5\,V/cm$. (Kolanoski 2016[14], page 126)

The drift movements of charge carriers lead to a drift current j_{drift}:

$$\vec{j_{\text{drift}}} = q\,n\,\vec{v_{\text{drift}}} \tag{2.14}$$

where n is the charge carrier density. This can now be identified with Ohm's law:

$$\vec{j_{\text{drift}}} = \sigma\vec{E} = q\,n\,\mu\,\vec{E} \tag{2.15}$$

which shows that the electrical conductivity is dependent on charge carrier density and mobility.
As mentioned in Chapter 2.3, charge carrier density in a homogeneous material is predetermined by doping concentration. It should be considered that Equations 2.12 to 2.15 stand for both electrons and holes, so they have to be summed up for a complete approach.

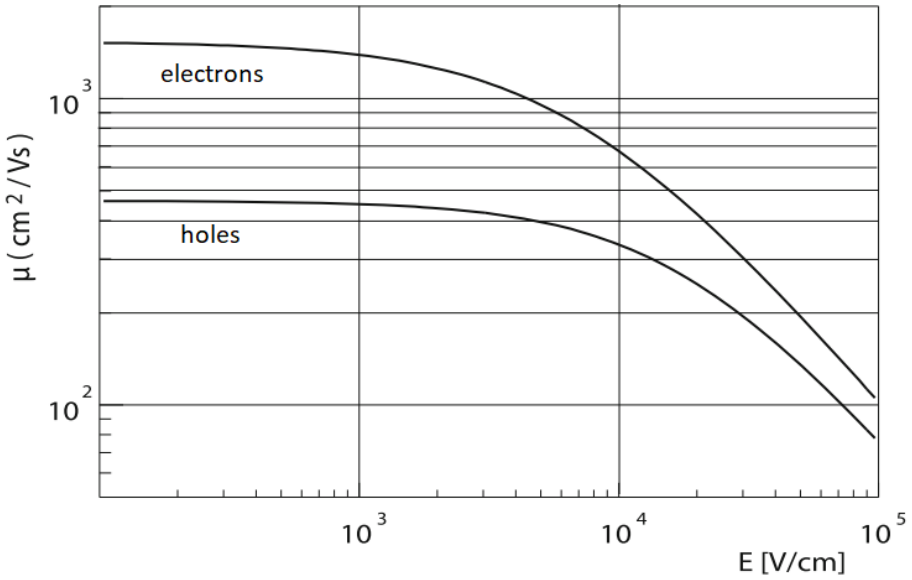

Figure 2.10.: Mobility of charge carriers in silicon at 300 K (Kolanoski 2016[14])

2.3.2. Diffusion

In homogeneous matter containing charge carriers, spatial charge concentration gradients tend to get compensated through thermal movement and Coulomb forces. According to Fick's first law of diffusion, this leads to a compensating current j_{diff} until a steady state is reached:

$$\vec{j_{\text{diff}}} = -e\,D\,\vec{\nabla} n \tag{2.16}$$

where D is the diffusion coefficient of the associated charge carrier and n its density. Note that in contrast to Equation 2.14, the current direction is independent of the charges' sign, because diffusion currents are always diametrical to concentration gradients.
Adding Equations 2.15 and 2.16 results in total currents of charge carriers:

$$\begin{aligned} \vec{j_e} &= -e\mu_e n_e \vec{E} - e\,D_e \vec{\nabla} n_e \\ \vec{j_h} &= e\mu_h n_h \vec{E} - e\,D_h \vec{\nabla} n_h \end{aligned} \tag{2.17}$$

In an one-dimensional (e.g. through a planar p-n junction) thermal equilibrium there is no net current, hence for electrons $j_e = 0$ (Kolanoski 2016[14], page 127):

$$\mu_e n_e E_x = -D_e \frac{\partial n_e}{\partial x} \tag{2.18}$$

An important connectivity between D and μ is given by the Einstein relation (Kolanoski 2016[14], page 128):

$$\frac{D_i}{\mu_i} = \frac{k_{\text{B}} T}{e} \tag{2.19}$$

where k_{B} is the Boltzmann constant and T the Temperature.

2.3.3. Doping and p-n junction

Adding foreign atoms to the semiconductor (doping) changes its electrical properties dramatically. Its most important effect is the change of charge carrier concentration. A dopant is characterized by its group in the periodic table. As typical semiconductors (silicon, germanium, diamond, silicon carbide) are in group IV, the most common dopants are acceptors from group III and donators from group V elements. Acceptor dopants (less electrons in the outer shell than the initial semiconductor, lowers Fermi energy) define p-type semiconductors, whereas donators (more electrons in the outer shell, increase Fermi energy) define n-type semiconductors. Typically for "light" doping, one dopant atom per 10^8 atoms is added. When the concentration is much higher, it is called "heavy" doping, denoted by a superscript $^+$, e.g. n^+ or p^+.
When contacting a p- and n-type semiconductor, a p-n junction or diode is established (see Figure 2.11). Electrons of the n-doped side diffuse into the p-type, whereas holes of the p-type move to the n side. At the junction region, electrons and holes recombine and a region with few free charge carriers is created: The depletion zone, which acts as an isolator. This creates an intrinsic electric field, which causes a drift current i_{drift} antiparallel to the diffusion current i_{diff}. In a thermal equilibrium they compensate each other. When applying a positive bias voltage (forward bias) from p to n side, the drift current

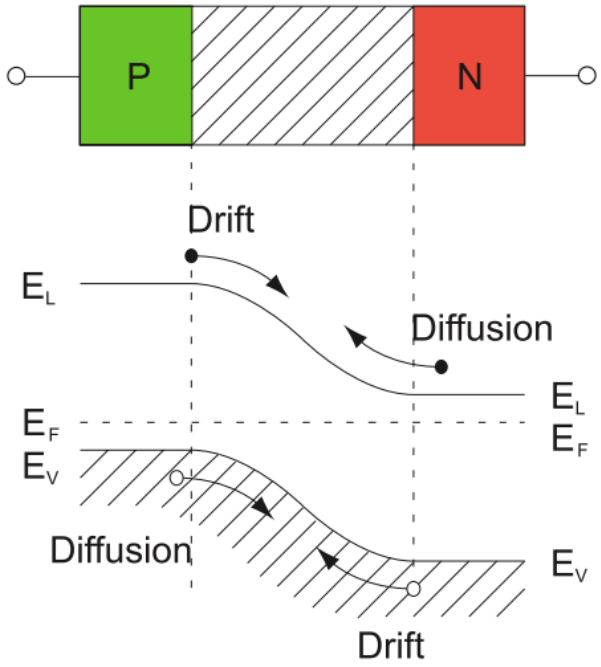

Figure 2.11.: Drift and diffusion at a p-n junction (Kolanoski 2016[14])

is increased compared to the diffusion current, so the depletion zone shrinks. By reduced depletion zone, the p-n junction loses resistance, so the forward current increases. This

behavior is described by the Shockley equation:

$$I(U) = I_0 \left[\exp\left(\frac{eU}{k_\mathrm{B} T} \right) - 1 \right] \tag{2.20}$$

whereas e is the elementary charge, U the forward bias voltage and I_0 is the reverse bias saturation current (the current that flows at reverse bias voltage, but before breakthrough).
By applying a negative bias voltage (reverse bias), the opposite situation is established: The depletion zone grows, which leads to a higher resistance (Kolanoski 2016[14], page 285ff). Further increasing the reverse bias may lead to a breakthrough, which can destroy the diode if there is a power supply with doesn't limit current flow.
As mentioned in Chapter 2.1.3, ionizing particles create electron-hole pairs, e.g. silicon needs 3.65 eV. A detector requires a charge-free region, as the charges should only be created by ionizing particles. In order to optimize the properties of the detector, a reverse bias high enough to fully deplete the p-n junction is required. This also minimizes the diode's capacitance, since a diode can be modeled by a parallel plate capacitor (the depletion zone acts like a dielectric).

2.3.4. Signal generation, analog readout and signal processing

As mentioned in Chapter 2.1.3, incident high-energy particles transfer momentum to detector electrons which results to an energy loss. This causes electrons to move into the valence band, equivalent to the creation of electron-hole pairs. These charge carriers can now move freely through the semiconductor and drift towards the electrodes due to the applied reverse bias voltage (see Figure 2.13). This induces a current pulse; its integral over time gives the charge deposition.
The amount of charge carriers received by the electrons do not cause current generation; the instantaneous change of electrostatic flux lines which end on the electrodes does (Ramo 1939[18]). The Shockley-Ramo theorem states that the instantaneous current j induced on a given electrode due to the motion of a charge is given by:

$$j = q \cdot v \cdot E_v \tag{2.21}$$

whereas q is the electric charge, v the instantaneous velocity and E_v the component of the electric field in the direction of v.
As seen in Equation 2.21, the electric field generates the drift movement of charge carriers. Subsequently for high current pulses, high fields (by applying a high reverse bias voltage) are crucial. High E fields also improve response times through increased mobility, as well as improved charge collection efficiency (Spieler 2005[19], page 55).
As seen in Figure 2.12, the detector current is transferred outside of the detector by either AC or DC coupling and amplified by a preamplifier afterwards, which is necessary for the next processing stage, the shaper.

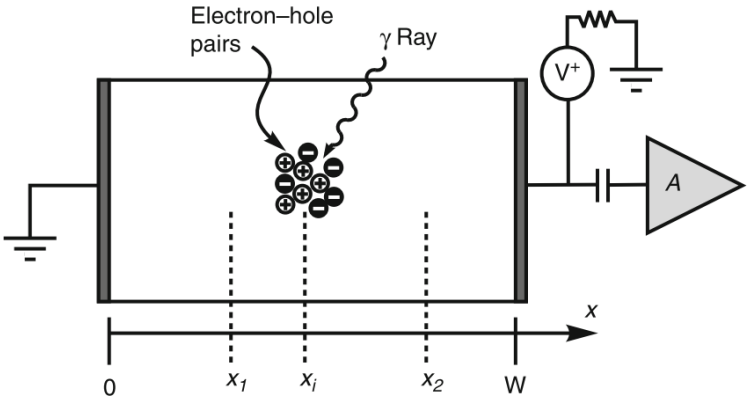

Figure 2.12.: Detector diode and preamplifier (Grupen 2005[20])

2.3.5. Segmentation and silicon strip sensors

Dividing a sensor module in many separate unities and readout channels provides many advantages:

- Higher spatial resolution, not only through higher amounts of detector elements, but also through charge sharing effects (only valid for analog readout, see Chapter 2.3.6).
- Reduced particle rate per readout channel.
- Distinguishing multiple tracks. Especially useful for jets, common in hadron collisions.
- Reduction of area per electrode leads to lower capacitance and electronic noise.
- Improved radiation hardness through smaller leakage currents.

One way for segmentation is to form long but narrow strips of diodes (see Figure 2.13) like for the Outer Tracker of the CMS detector (see Figure 1.6). The detectors used in this work are strip sensors.

2.3.6. Charge sharing and eta value

In segmented silicon sensors, maximum achievable spatial resolution is not only given by segment distance: If a particle hits the area between two segments (most particles will do that), the generated charge (e-h pairs) will drift to both adjacent segments. Assuming that the lateral segment geometry is symmetrical, the deposited charge should be distance proportional transferred to each segment. Now one can define (using the center of gravity method) the η value, for determining the hit position between the two segments. In case of 1-dimensional segmentation (strip sensors), η is defined as

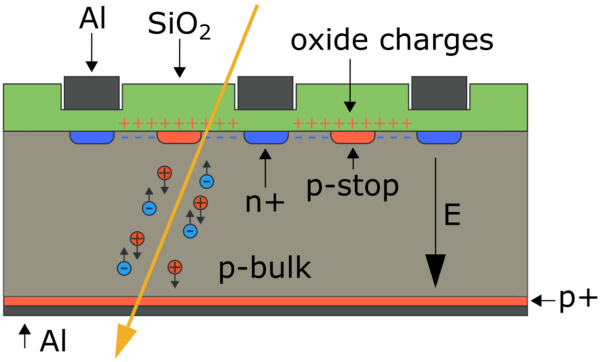

Figure 2.13.: Schematic view of a strip sensor with charge carrier generation by an incident high energy particle (Hinger 2017[21])

the weighted ratio between the charges collected by the "left" and "right" strip (Hinger 2017[21], page 55):

$$\eta = \frac{Q_L}{Q_L + Q_R} \tag{2.22}$$

If the strips are close enough, diffusion (see Chapter 2.3.2) and δ-electrons will lead to charge sharing over multiple strips. This will occur if the dimensions of the generated charge cloud are in the same (or larger) scale as the distance between the strips. By implication, the center of gravity method for determining the hit position is also working in this case by summing up over all cluster strips:

$$y = \frac{\sum_{i=0}^{n} Q_i \cdot y_i}{\sum_{i=0}^{n} Q_i} \tag{2.23}$$

where n stands for the size of the cluster, y_i is the center position of the strip with index i, and Q_i gives the collected charge for strip i.
Spatial resolution using analog readout systems and charge sharing is given by

$$\sigma_x^2 = \frac{1}{p}\int_{-\frac{p}{2}}^{\frac{p}{2}} x^2 dx = \frac{p^2}{12} \qquad \longrightarrow \qquad \sigma_x = \frac{p}{\sqrt{12}} \tag{2.24}$$

whereas p is the strip pitch (König 2017[22], page 32).
It has to be mentioned that charge sharing is also induced when a particle hits the sensor with a trajectory not perpendicular to the surface, by hitting multiple strips, a bigger cluster is generated. That can be the case in an externally applied magnetic field which bends the particle trajectory. At testbeam environments discussed in this thesis, the incident particle trajectories are considered to hit the sensor plane almost perpendicularly, because the sensors were not rotated in the beamline.

3. Experimental Setup and Preparatory Tests at HEPHY

3.1. Principles of testbeam setups

3.1.1. Telescope

Main goal of testbeam setups is to verify the functionality of a device under test (DUT, in most cases a particle detector prototype), electronics, data acquisition (DAQ) or triggering systems. Noise is characterized by stochastic fluctuations, but beam trajectories are deterministic. To distinguish between desired particles (e.g. coming from the accelerator) and unrequested particles (e.g. cosmic radiation and background radioactivity, but also particles leaving the setup through scattering), for efficiency tests, geometrical analysis, tracking and alignment, multiple detector planes are crucial, so a "telescope" is used to reconstruct particle tracks. Figure 3.1 shows a schematic view of a typical telescope setup.

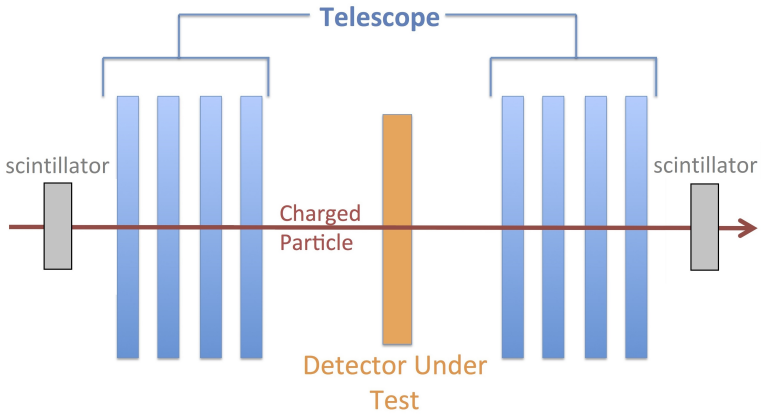

Figure 3.1.: Telescope setup with trigger scintillators for testbeams (QD[17], 2017/07)

3.1.2. Triggering and data acquisition

For triggering, one can distinguish between external triggering (when particle emit times are known, e.g. in synchronous pulsed sources like the experiments at LHC) and self triggering by trigger elements. In a typical testbeam environment a self triggering system is installed (see Figure 3.1, usually by scintillators connected to PMTs, see Chapter 3.2.1). In order to reduce undesired triggering, a trigger is usually only fired when a particle hits

all triggering scintillators. This can be achieved by using a coincidence circuit, consisting of logical AND gates: $A \wedge B \wedge C$. Therefore a trigger is only fired and redirected to the DUT if all detectors A,B and C are firing simultaneously. "Simultaneously" in this case is given by a timing frame, triggered by the first hit. If all three triggers are fired during this time period, the coincidence circuit passes the trigger signal directly to the DUT or to a TLU (trigger logic unit). To reduce false trigger events, the time frame should be much smaller than the expected mean time between two incident particles.
To reduce noise from unwanted particle trajectories, it is also possible to add a veto element, e.g. a scintillator with a hole (where the beam should pass) and subsequent NOT-logic (Kolanoski 2016[14], page 523): $A \wedge B \wedge C \wedge \overline{R}$
In a modern tracking system, hierarchical data acquisition (DAQ) steps are distinguished:

- When a particle passes all scintillator planes, ideally a trigger signal is fired. This is passed to the DUT, which in turn produces an event and the readout system records channel data.
- During the analysis, each event is scanned for correlated clusters (one particle can induce a signal in more than one channel). Noise contribution is processed by using pedestals and subtracted from the overall signal.
- After identification of clusters, a hit is generated. A hit contains all information regarding cluster size, energy deposition, spatial and temporal descriptions.
- By comparing hits and considering telescope geometry (6 coordinates per detector plane: 3 translations and 3 rotations) the alignment software calculates the relative position of the detector planes in a defined coordinate system. Usually it is done via an optimization algorithm iteratively until convergence and/or a defined number of iterations.
- When the alignment is finished, a tracking algorithm should be able to reconstruct particle trajectories through the testbeam setup.

3.2. Experimental setting

3.2.1. Scintillator system

Each scintillator triggering system consisted of a fast timing anthracene-doped polyvinyltoluene (PVT) scintillator Eljen EJ-230, connected via an Eljen polymethyl methacrylate (PMMA) lightguide to a Hamamatsu photomultiplier tube. The scintillators and lightguides were covered light-tight by a black adhesive tape. Power supply was provided by a CAEN SY5527LC rack housing a CAEN A1517B board. The signals were guided via LEMO coaxial connectors to a NIM crate with dedicated trigger elements at the MedAustron test sites, to an integrated TLU at DESY, or directly to the TRIGGER IN input of the ALiBaVa mainboard (see 3.2.2) for the lab experiments.

3.2.2. Strip sensor readout: The ALiBaVa system

Due to the attended non-consecutive night shifts of six hours of beam time at the MedAustron test beam site, an uncomplicated and robust setup was preferred, fulfilled by the ALiBaVa System Classic (see Figure 3.2). Its main components are the motherboard which contains an ADC (analog to digital converter), external trigger inputs and the daughterboard hosting a silicon strip sensor DUT (device under test) and an analog Beetle chip (Löchner 2006[23])for readout. It was originally developed for the LHCb experiment, so this chip features a 40 MHz clock, synchronized to the 40 MHz bunch clock at the LHC (see Table 1.1). A list of used sensors at the test beam sites is given in Table 3.1 (ALiBaVa manual[24]). Unlike the synchronous triggering clock at LHC, the ALiBaVa system is designed for asynchronous triggering by polling the trigger input every 25 ns (chip clock cycle). If a trigger is registered, a time frame of 100 ns (4 clock cycles) is available for pulse shaping in order to measure the full pulse. Power supply

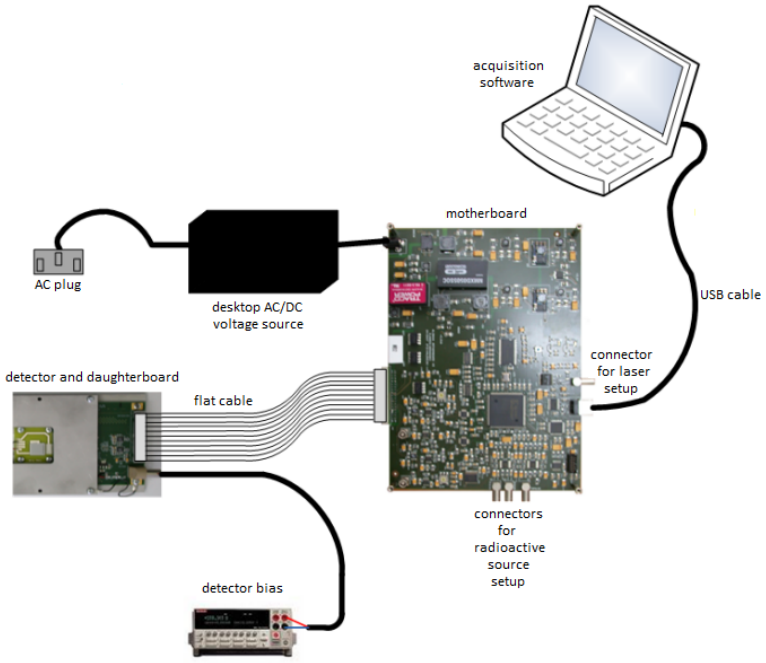

Figure 3.2.: Sketch of the ALiBaVa-System (ALiBaVa manual[24])

(reverse bias voltage) for the daughterboard sensor was provided by a Keithley Model 2410 SourceMeter.
The ALiBaVa open-source software features operation via a GUI (Figure 3.3), which runs on Windows, iOS and Linux. Alternatively, it can be accessed via command line, but monitoring possibilities and usability is limited.

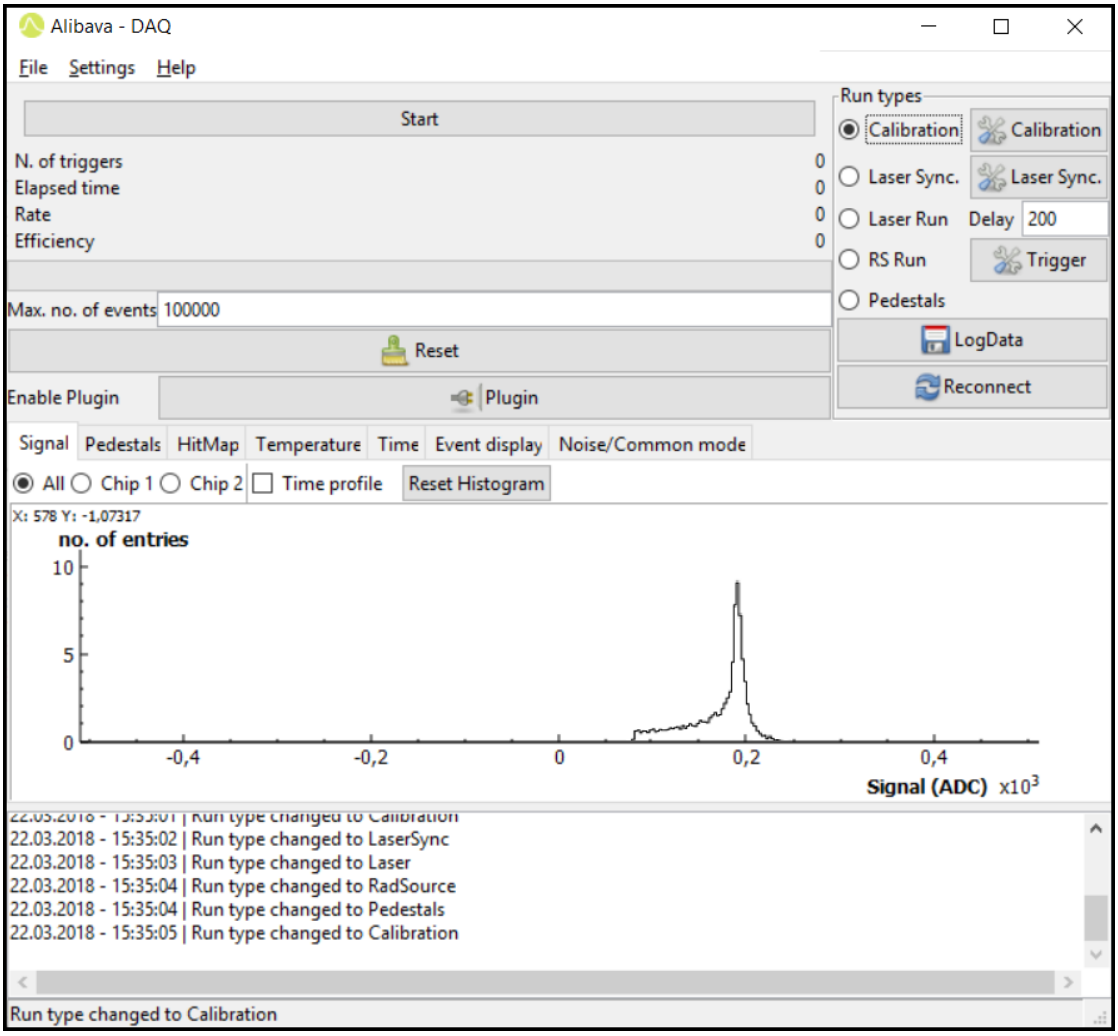

Figure 3.3.: Screenshot of the ALiBaVa GUI

Operational modes of the ALiBaVa system

The ALiBaVa software provides five different run modes, which usage depends on the testing environment (ALiBaVa user manual[24]):

- **Pedestals:** Performs a pedestal run. Alibava generates an internal trigger that will allow to compute the baseline or pedestals and its variation (the noise).
- **Calibration:** Initiates a calibration run. ALiBaVa programs the Beetle (Löchner 2006[23]) chip to inject calibration pulses to all channels in order to characterize the electrical behavior of the ASICs. To form a well-defined pulse, a capacitor is charged to a reference voltage. Then it is discharged to generate a defined current pulse. After the pulse, the corresponding ADC counts are measured. This cycle is repeated for multiple charges to obtain a charge-to-ADC count mapping.

- **Laser Sync:** Laser synchronization. ALiBaVa is able to send a pulse that can be used to trigger a laser system. This run mode scans the delay between the pulse sent by ALiBaVa and the acquisition, so the system will sample at the maximum of the signal produced by the laser.
- **Laser Run:** Starts a laser run via an external laser. As well as charged particles, laser pulses can be used to generate signals in silicon sensors (see Chapter 3.4.3). One needs to run in laser synchronization mode before reading back the optimal signal produced by the laser.
- **RS Run:** Radiation source run. This run mode is used for data runs, using a radioactive source or testbeams. It performs a run in which the acquisition is triggered by signals above the threshold of the input connectors.

During data acquisition, the ALiBaVa GUI provides useful online monitoring tools: Trigger efficiency, signal histogram (entries per ADC counts), pedestals, a hitmap (entries per channel), temperature, monitoring of pulse shaping, noise and common mode recording.
For offline analysis (after the testbeams), a full (but without tracking) hit reconstruction software stack is provided: Cluster analysis, gain characteristics, common mode correction and pedestal subtraction, eta distribution (see Chapter 2.3.6), channel masking[a] and hitmaps, SNR measurements and signal histograms. The offline analysis tools have been previously modified and extended by Viktoria Hinger (Hinger 2017[21]). It was later extended to meet advanced requirements such as enlargement of the displayed ADC range, automation analysis macros for multiple testbeam runs and algorithms to compare different data runs.

3.3. Preparatory scintillator tests

3.3.1. Dark rate determination

A primary quality characteristic of triggering systems based on scintillators is the dark rate. It is determined by the control voltage, light shielding and other parameters. The dark rate is defined by the number of counts the detector produces in absence of any radiation source, so it is mainly composed of electronic noise and diffused light from outside. In lab conditions, there are always additional sources of ionizing radiation (like cosmic muons or natural radioactivity), which are added up to the dark rate. In case of a leaky light shielding, external light sources like artificial lighting or daylight will lead to a higher "dark" rate. This has to be avoided to prevent random false triggers. The light shielding was applied by a black duct-tape wrapping.
First tests showed a significant difference between the two scintillators (see Figure 3.4). Scintillator 1 had a dark rate about 10 times higher than scintillator 2. When covered with a blanket and without lab lighting, the dark rate became comparable to scintillator

[a] masking: excluding hot strips from the analysis

2. This indicated a leaky light barrier. After renewal of the tape, both scintillators showed similar dark rates (see Figure 3.6).

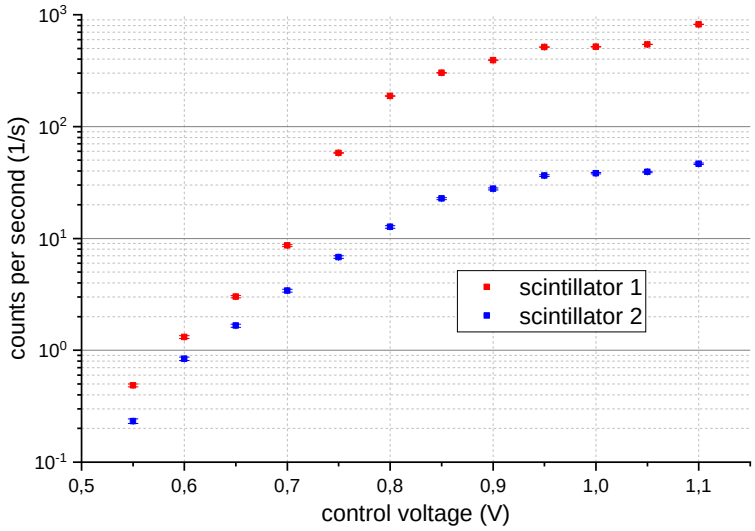

Figure 3.4.: Early test of scintillator 1 showed bad tape shielding

3.3.2. Radioactive source tests with ^{90}Sr

To ensure functionality of the scintillators, tests using a 295 µCi ($1.09 \cdot 10^7$ Bq, July 2017) ^{90}Sr source in the electronics laboratory at HEPHY were conducted. This isotope itself has a β-electron energy up to 0.546 MeV, which is too low to reach both the sensor through the light shielding and the subjacent scintillator. However, its daughter nuclide ^{90}Y has a β-electron energy up to 2.28 MeV, sufficient for penetrating the sensor and scintillator (IAEA:NDS[25], 2018/01).
To investigate geometrical dependencies of the scintillator, a coordinate system was defined (see Figure 3.5), where the origin is equal to the center of the scintillator area. The X-axis heads towards the photodiode, while the Y-axis defines the lateral distance to the center. X- and Y-axes are in the scintillator plane, while the z-axis is parallel to the incident beam. Measured count rates by using a β-radiation source showed expected performance: Higher control voltage lead to better efficiency, but also an increased dark current (Figure 3.6).

To test homogeneity of the scintillator area, the beam of the radiation source was positioned at different locations over the surface.

As to be seen in Figure 3.7, the lateral y-axis reveals minor variations over its width. Fluctuations over the active scintillator region are considered to be caused by uneven distribution of the tape wrapping. The longitudinal x-axis shows a drop when getting closer to the light guide. According to the underlying physics, the light guide itself should not show scintillation effects by β-radiation, so the small signals at 35 and 40 mm are

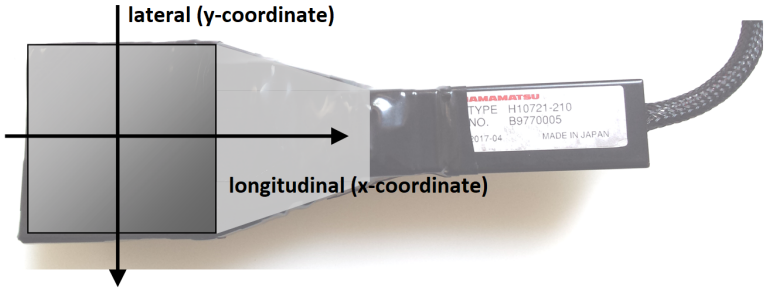

Figure 3.5.: Coordinate system of the scintillator tests, viewpoint from the radiation source. The dark gray area identifies the active scintillator region, whereas the light grey area marks the lightguide.

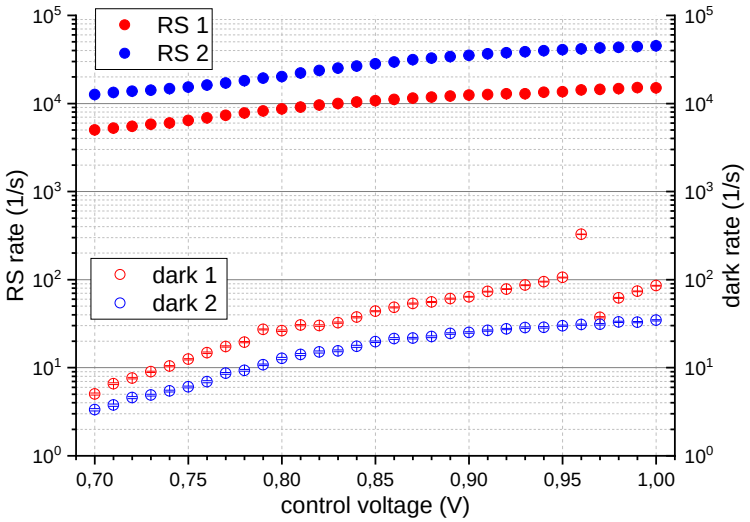

Figure 3.6.: Dark rate versus radiation source rate for both scintillators used at MedAustron TB 1

considered to be caused by scattered electrons and geometrical spreading of the incident beam cone. The position uncertainties are mainly given by the visual alignment of the beam.
As the β-radiation of ^{90}Sr has an energy spectrum orders of magnitudes smaller compared to testbeam particles, the light shielding of duct-tape layers imply an inevitable attenuation of the radiation. To quantify these results, additional layers of tape were placed on one scintillator to measure the increased absorption. Regression analysis was consistent to the Beer-Lambert law (Figure 3.8) with an exponential decrease in intensity at thicker tape layers.

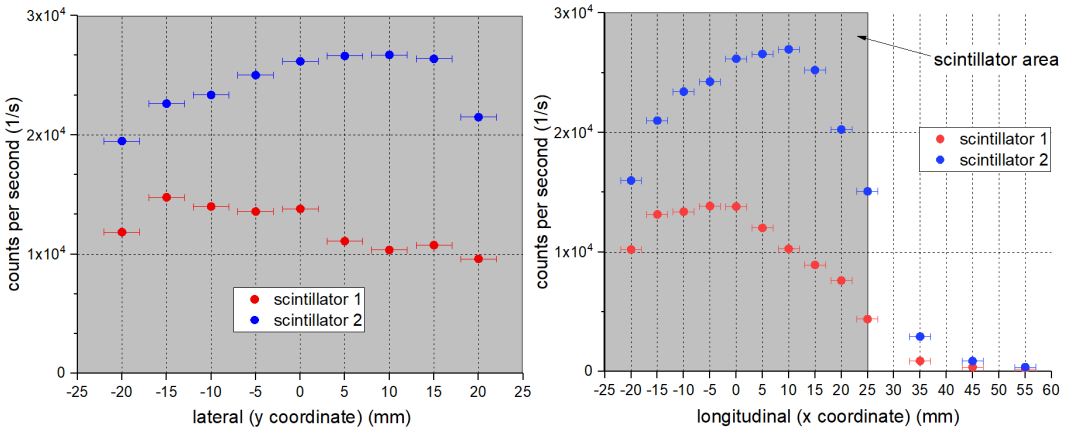

(b) Longitudinal distribution

Figure 3.7.: Geometry scans of scintillators used at MedAustron TB 1. The grey area marks the active scintillator zone.

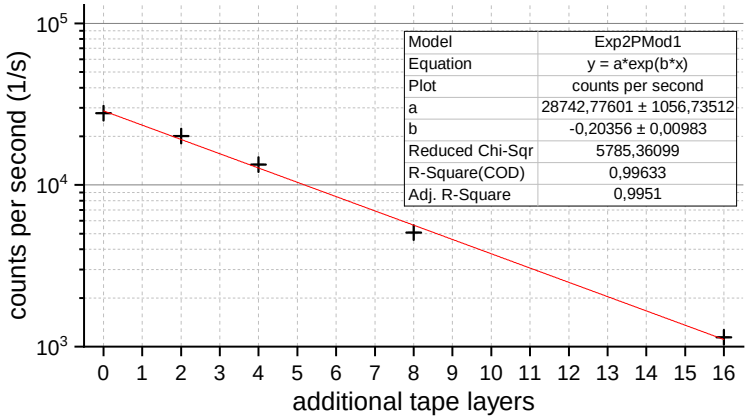

Figure 3.8.: Count rates at additional layers of light shielding tape applied to the scintillators

3.4. Preparatory strip sensor tests

In order to prove functionality in preparation to the testbeams, the strip sensors had been tested at HEPHY. The tests embraced IV-characteristics, radioactive source and laser tests. Table 3.1 shows a summary of the utilized HEPHY sensors, certain physical characteristics and their application at testbeams. At DESY four additional sensors from Karlsruhe Institute of Technology were tested (see Chapter 3.7).

[b]König 2017[22], Table 4.2

sensor ID	pitch (µm)	strip length (cm)	strips	physical thickness (µm)	active thickness (µm)	testbeam
IFX Baby	90	5.09	254	200	200	MedAustron 1
IFX Irrad	90	2.27	127	200	200	MedAustron 2
IFX CenterBias	90	1.12	254	200	200	DESY
HPK CenterBias	90	1.12	254	320	240	DESY

Table 3.1.: Parameters of HEPHY strip sensors[b], ulitized at the testbeams.
HPK = Hamamatsu, IFX = Infineon

3.4.1. IV characteristics

In order to check functionality and performance of the utilized sensors, the first step was to measure IV characteristics, which can give indications about full depletion voltage. For a precise determination of depletion, a CV curve would be more significant but to obtain it on already bonded and assembled modules was not possible. However, leakage current could be measured, which is a basic indicator of strip sensor quality. Figure 3.9 compares the sensors used at the MedAustron testbeams. Full depletion voltage was (previously determined) at approximately 70 V. When observing the reverse current, one may note that the larger IFX Baby shows about 3.5 times more than the IFX Irrad. As seen in Table 3.1, the IFX Baby's active area (length · pitch · N_{strips}) is 4.48 times higher than of IFX Irrad, which explains the higher leakage current.

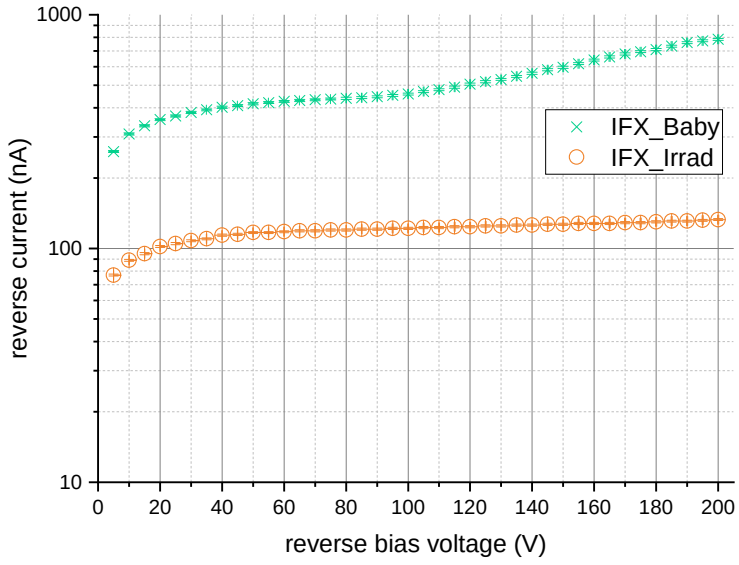

Figure 3.9.: I-V characteristics of the sensors used at MedAustron testbeams

3.4.2. Radioactive source tests

In addition to the scintillators (Chapter 3.3.2), all the strip sensors used at the testbeams were checked for functionality using the radiation source. A simple external triggering system was established by a scintillator placed after the sensor, which was directly connected to the trigger input of the ALiBaVa motherboard. Figure 3.10 shows the signal spectrum of the strip sensors irradiated with the ^{90}Sr source in a low electronic noise environment at HEPHY. The mean is at approximately $3 \cdot 10^4$ electrons, which is equivalent to a deposited energy of 109 keV. At the left flank of the Landau profile, a small noise peak is visible. Since the β-particles are not monoenergetic but have an energy

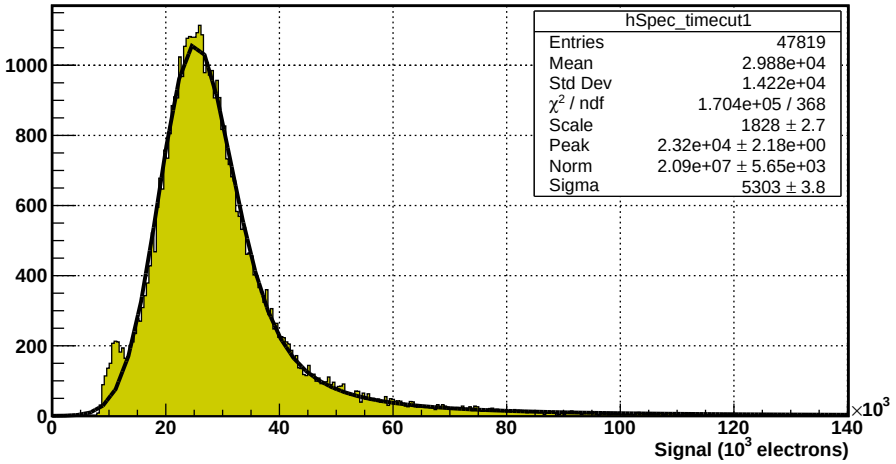

Figure 3.10.: Histogram of the signal of a preparatory test run using the ^{90}Sr source. Sensor: IFX Baby, U_{bias} = -100 V

spectrum, this distribution is the sum of many single Landau profiles adding to the visible Landau-like profile, so it is not useful as measurement of the β-energy spectrum. In addition to the β-electrons of ^{90}Sr and ^{90}Y, γ-photons (1.7 MeV) of the daughter nuclide contributed to the spectrum. However, ^{90}Sr is a useful tool to test overall functionality and SNR.
To quantify ALiBaVa's maximum processable particle rate, the radioactive source was directed to the IFX Baby at different distances, varying the particle rate ($1/r^2$ law). It turned out that the system's maximum rate is about 600 Hz on average, but allowing bursts in the lower kHz range.

3.4.3. Laser tests in the clean room

To determine the upper energy deposition limit of the sensor (which is important for high particle rates at MedAustron), a laser test stand in the clean room at HEPHY was used. The laser itself is installed in a light-tight safety box with an interlock system to avoid eye injuries through direct or scattered laser light.
The system (Hinger 2017[21], page 26) consists of a near-infrared picosecond diode laser

PiLas PiL106X and a mounting table which can be remotely moved in all (x-y-z) directions via a computer. A voltage-controlled attenuator (Thorlabs V1000A) is connected via single mode fibers between the laser diode and the lens system. This allows to vary the laser output intensity from outside the laser box. The laser tests at HEPHY demon-

Wavelength	1055.6 nm
Spectral width	7.8 nm
Pulse width	50 ps
Maximum repetition rate	40 MHz
Maximum pulse energy	8 pJ
Minimum beam spot diameter	4 µm

Table 3.2.: Parameters of the laser system (Hinger 2017[21])

strated the upper dynamic range of the readout system. Laser pulse intensity was varied in steps, and data runs were taken at each step. Figure 3.11 shows signal histograms at two different laser pulse intensities: The low intensity released an energy equivalent of $1.88 \cdot 10^4$ electrons, the high intensity pulses $2.51 \cdot 10^4$ electrons. It is clearly visible that with increasing pulse energies the Gaussian distribution widened and its center was moving to higher energy depositions. As the profile was spreading out, the peak height was decreased. So at very high intensities it was difficult to recognize the peak, because it got smeared out and deformed and therefore the shape of the Gaussian profile was hard to identify.
Saturation was reached at approximately $6.4 \cdot 10^5$ electrons, but this should not be seen as the actual upper energy deposition limit of the sensor. In fact, it shows the upper limit of the dynamic range of the Beetle chip. In this region, hits were still displayed, but as mentioned before, this signal magnitudes are far beyond the linear range and not suitable for actual testbeams. A MIP (Minimum Ionizing Particle) releases about $\approx 2.13 \cdot 10^4$ electrons in 200 µm active thickness (Kolanoski 2016[14], page 315). Since functionality in the interesting linear range and its limits were confirmed, these tests were not continued or expanded by reasons of time.

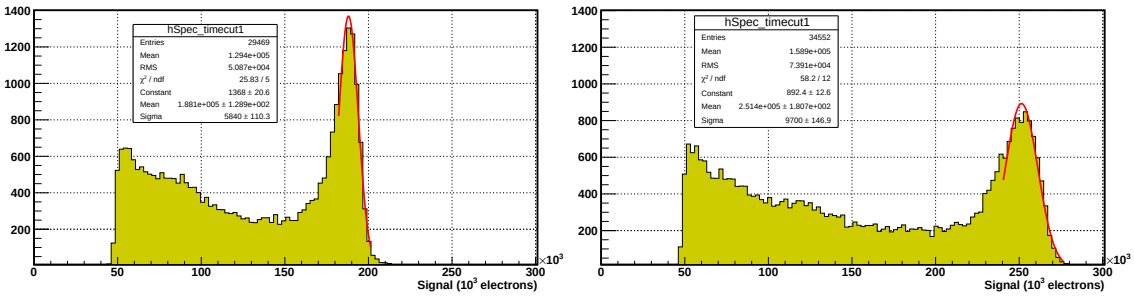

Figure 3.11.: Signal histogram of laser tests. Left: low intensity, right: high intensity Sensor: IFX Irrad, U_{bias} = -150 V

3.5. Proton testbeam 1 (TB 1) at MedAustron

The first testbeam at MedAustron facility was carried out by utilizing a "classic" trigger layout, with one scintillator in front and one after the device under test (DUT, see Figure 3.12). The distance between the accelerator's polyimide outlet window and the first scintillator was $d = 50\,\text{cm}$. The trigger signals were directly fed to NIM-modules (LeCroy 821 Quad Discriminator, CAEN N405 Logic Unit and a CAEN scaler N1145). The output of the coincidence was fed into the EXTERNAL TRIGGER IN of the ALiBaVa mainboard.
Since the beam spot has a FWHM of 4-10mm at lowest energy (see Chapter 1.4), the large strip sensor IFX Baby (Table 3.1) was used.
Before conducting the first testbeam, particle rates were expected to be directly controllable, comparably to other testbeam sites. During TB 1 it became clear that just the extraction time could be varied, and not the particle rate (which, of course, is sufficient for patient treatment purposes). Effective particle rates were between 10^8/s and 10^{10}/s.
Data acquisition was primarily taken over by the ALiBaVa readout system through a connected DAQ PC, remote-controlled over Ethernet via SSH and VNC.
Data transfer was achieved by connecting the ALiBaVa motherboard to a DAQ-PC via USB. This PC was remotely controlled via SSH and VNC. The DAQ-PC also operated the SMUs for power supply of the PMTs and the DUT. This allowed online monitoring of the data via the ALiBaVa-GUI, including trigger efficiency, histograms of the analog signal height and hitmaps.
Monitoring the LED indicators of the SMUs and NIM modules happened via webcams, provided by MedAustron.

run ID	**energy (MeV)**	**intensity (s^{-1})**	**events**
run003_1E8	62.4	10^9	714845
run008_1E8	97.4	10^9	464474
run006_1E8	148.2	10^9	582050
run007_1E8	175.3	10^9	605763
run005_1E8	198.0	10^9	226880
run002_1E8	252.7	10^9	319445

Table 3.3.: Overview of usable data runs at MedAustron TB 1

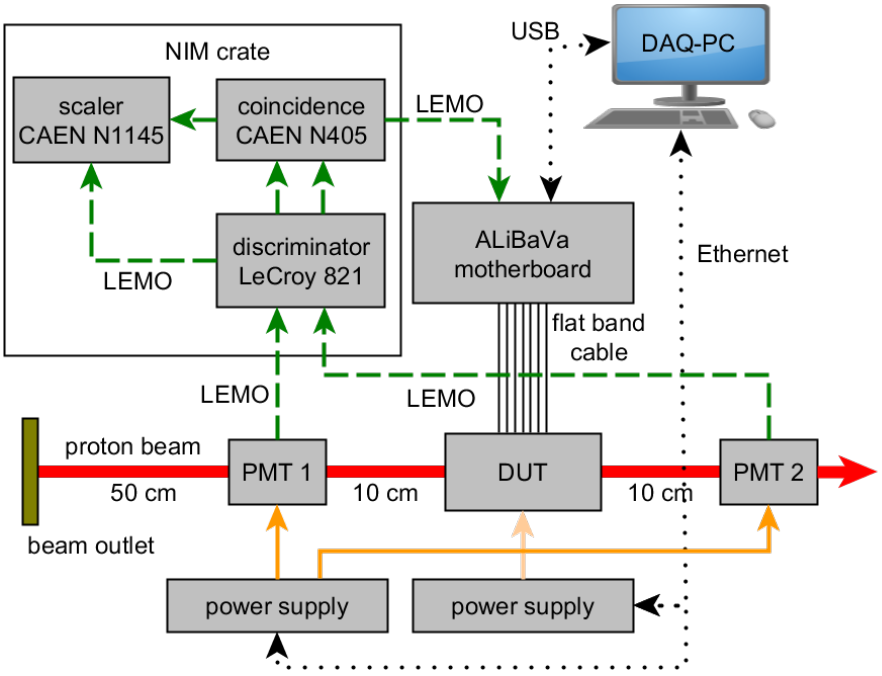

Figure 3.12.: DAQ, triggering and power supply at MedAustron TB 1. Continuous yellow lines are power supplies, dashed green lines are trigger signals over coaxial cables and dotted black lines are signal and digital data connections

3.6. Proton testbeam 2 (TB 2) at MedAustron

During data analysis after TB 1, it became clear that particle rates of 10^8/s or higher lead to pile-up effects, which negatively affected energy and spatial resolution. To encounter this problem, several changes based on predefined recommendations (L. Badano, S. Rossi 2006[26] and Jan Borburgh, T. Kramer 2012[27]) to the synchrotron were made by MedAustron staff. Detailed information of applied methods and results have not been published yet (2018).
To improve energy resolution at lower energies, the setup was altered by placing all scintillators after the DUT and decreasing distance to the beam outlet window (see Figure 3.13).
For trigger control, a triggering system using a FPGA board was provided externally by Alexander Burker and Felix Ulrich-Pur. It was composed of a CAEN V2718 VME-PCI Optical Link Bridge, a CAEN V895 Discriminator and for DAQ and control a CAEN V2495 Programmable Logic Unit. Coincidence was established by the FPGA.
It was assumed that the smaller strip sensor IFX Irrad (Table 3.1) would have less occupancy and less noise contribution than the IFX Baby, so this sensor was used at the testbeam.
As in TB 1, monitoring the LED indicators happened via webcams.

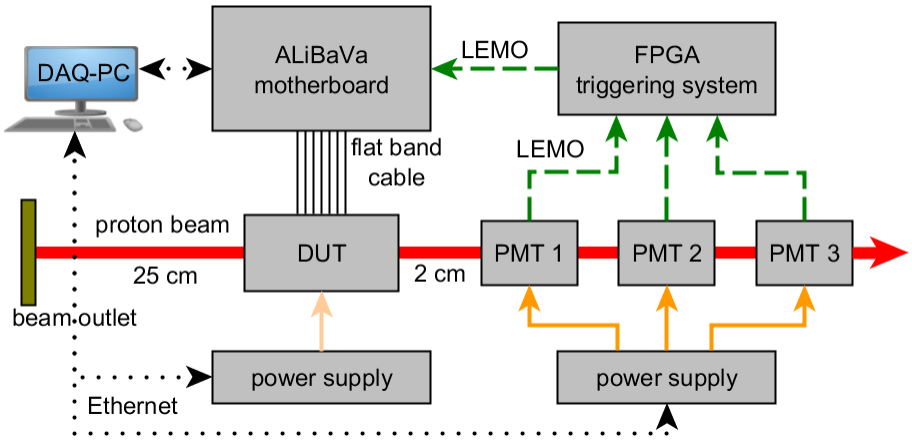

Figure 3.13.: DAQ, triggering and power supply at MedAustron TB 2. Continuous yellow lines are power supplies, dashed green lines are trigger signals over coaxial cables and dotted black lines are signal and digital data connections. The triggering system was provided externally.

run ID	**energy (MeV)**	**intensity (s^{-1})**	**events**
run010_1E5	62.4	10^5	100000
run011_1E9	62.4	10^9	101000
run009_1E5	83.0	10^5	101000
run007_1E4	100.4	10^4	20000
run008_1E5	100.4	10^5	200000
run005_1E5	145.4	10^5	115599
run006_1E5	145.4	10^5	100000
run004_1E5	175.3	10^5	200000
run003_1E5	194.3	10^5	200000
run002_1E4	252.7	10^4	50000
run001_1E5	252.7	10^5	200000

Table 3.4.: Overview of usable data runs at MedAustron TB 2

At TB 1, it was observed via webcam that during the spills the LED for compliance of the bias supply SMU flashed up intermittent. This lead to the suspicion that the bias voltage of the sensor dropped during the spills, decreasing the depletion zone and reducing the signal height. To prove this assumption, the current flow of sensor's power supply had to be monitored.
In preparation to TB 2, a connection wire was soldered to the power supply circuit in the module casing. The potential was measured after the lowpass filter where fast fluctuations in the supply voltage were expected to be visible.
The measurement points were connected to a high-impedance (GΩ) probe for determining the current consumption, readout was achieved via a Keithley Model 2410 SourceMe-

ter using a DAQ software written by Johannes Grossmann. Current measurements were logged every 349 ms for resolving the short proton spills of approximately 1 s.

3.7. Electron testbeam at DESY

The setup at the DESY II synchrotron was more complex than that of MedAustron TB 1 and 2. A beam telescope (see Chapter 3.1) of the DATURA type, based on Mimosa26 pixel sensors was applied. A FEI4 pixel sensor plane was placed after the last telescope plane. It provided timing reference as well as a control window for region of interest scans. For rotation of the DUT, a rotatable and remote-controlled mount was applied to the telescope frame structure.
Two non-irradiated sensors from HEPHY were tested, as well as previously irradiated (25 MeV protons at KIT's cyclotron) sensors from KIT (see Table 3.5).
Figure 3.14 shows a simplified sketch of the overall setup. As a matter of lucidity, it doesn't show converters (like TTL/NIM), controllable power supply lines, cooling pipes (for the telescope and irradiated DUTs) and the rotation control. For further information, DESY provides excellent documentation and manuals of the telescope setup, data connections, hard- and software configurations at their website (DESY:Telescope[28]).

To provide best synchronization between telescope and ALiBaVa data streams, the buffer size (number of recorded events until readout) was equally set to 10^4. Because a few runs crashed (either the ALiBaVa and/or the EUDAQ software), it was mandatory to change the headers of the corrupted ALiBaVa data files. It was done by opening a non-corrupted file with a Hex editor and copying the intact header over the incomplete one of the corrupted file. It is important to change the number of events in the header to match data and header specifications. This method was also used to merge data run files at identical setups to provide better statistics.
At DESY, a total of 182 data runs with 77 million recorded ALiBaVa events were taken, with a duration of approximately 107 hours. 26 data runs were suitable for analysis, the others were alignment runs and efficiency tests, invalid data through thermal runaways (irradiated sensors), or corrupted files caused by software crashes. The HEPHY module tests generated in total 12 million recorded events in 17 data runs. In addition, four irradiated sensors from KIT (Karlsruhe Institut for Technology) were analyzed, which needed extra cooling to reduce leakage current and breakthroughs.

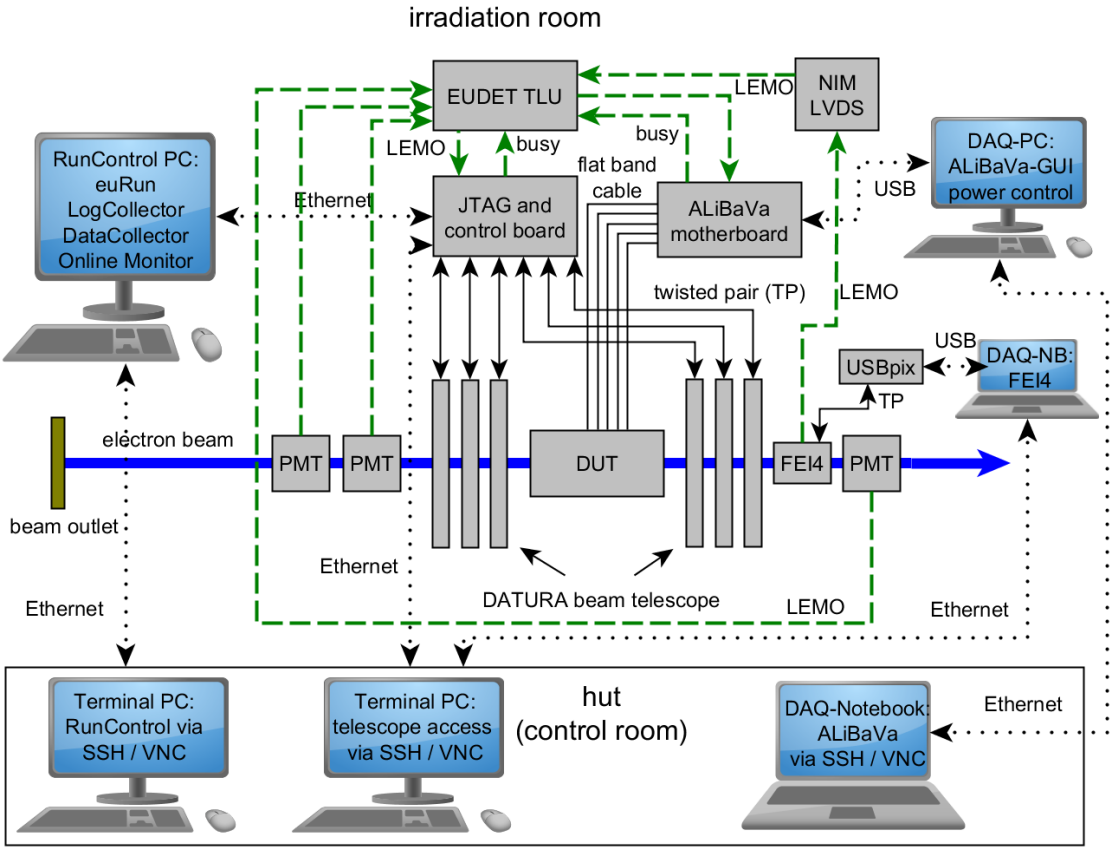

Figure 3.14.: Simplified sketch of DAQ and triggering at DESY. Dashed green lines are trigger signals over coaxial cables and dotted black lines are signal and digital data connections.

sensor ID	**owner**	**fluence Φ_{eq}**
HPK_CB	HEPHY	0
IFX_CB	HEPHY	0
HPK_200_3e14	KIT	$3 \cdot 10^{14}$
IFX_200_3e14	KIT	$3 \cdot 10^{14}$
HPK_200_1e15	KIT	$1 \cdot 10^{15}$
IFX_200_1e15	KIT	$1 \cdot 10^{15}$

Table 3.5.: Used strip sensors at DESY. HPK = Hamamatsu, IFX = Infineon. The sensors from KIT were irradiated previously at KIT by 25 MeV protons. Φ_{eq} is the equivalent fluence of 1 MeV neutrons

4. Testbeam Analysis and Results

4.1. Silicon sensor analysis

4.1.1. Noise and pedestal analysis

Figure 4.1 shows the noise spectra (histogram of counts per signal height in idle mode) of the IFX Baby module at preliminary tests at HEPHY and at MedAustron TB 1. The spectrum indicates an exponential drop for higher signals, however, modeling this behavior did not reflect an appropriate fit for analysis. Furthermore, convolution of a Landau/Gauss profile (signal) with an exponential decrease (noise) to fit the measurements did not perform as expected.

The term "pedestal" denotes the base line[a] of the signal. The pedestal's fluctuations are

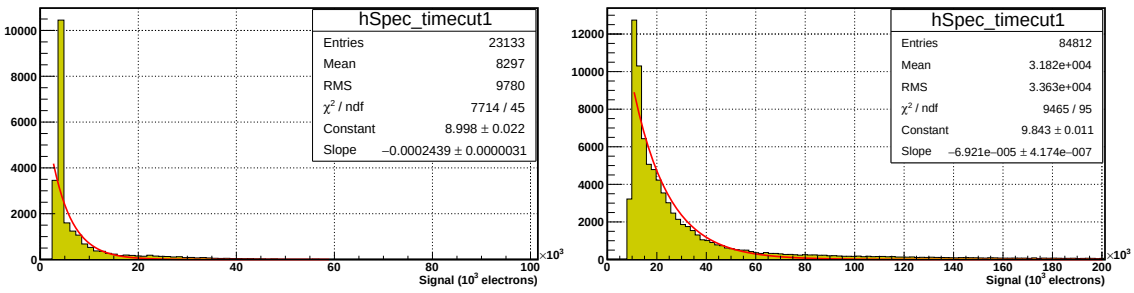

(a) HEPHY (b) MedAustron

Figure 4.1.: Noise spectra of HEPHY tests and MedAustron TB 1
Sensor: IFX Baby, U_{bias} = -100 V

identified with baseline noise. The ALiBaVa system provides an option to automatically correct the signal by measured pedestals and common mode noise[b]. Figure 4.2 is an example of the measured noise per channel. The applied IFX Irrad is composed of two separate chips, therefore one may note the plateau between channels 113 and 140. It is caused by the gap between the two parts of the sensor. Additional noisy channels can be found at 19, 101, 150 and 212, affecting also adjacent channels through cross-talk. To improve signal quality, it is crucial to mask the noisy channels, in other words to exclude them in the analysis.

It has to be noted that the sequence of the channel number is not equal to the geometrical sequence of strips, caused by different bonding schemes. To perform analysis, one

[a] signal that is measured when no incident particles hit the sensor

[b] interference equal on signal and circuit return

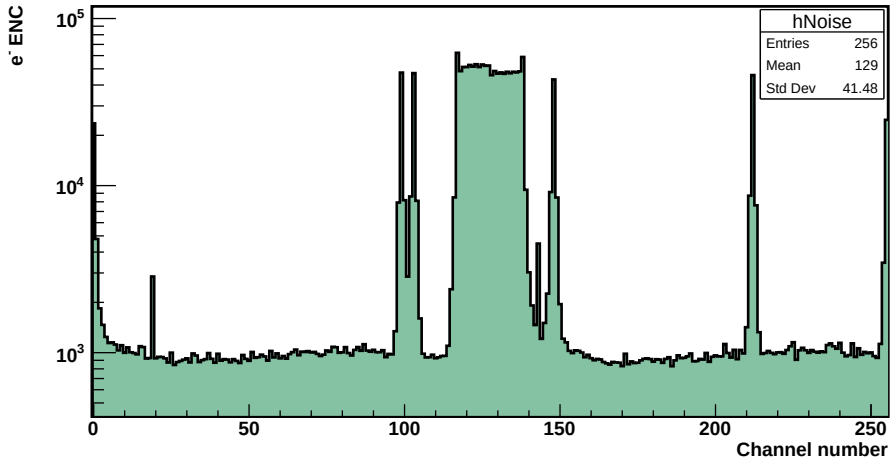

Figure 4.2.: Noise per channel of MedAustron TB 2. Sensor: IFX Irrad

has to do a channel to strip mapping (or vice versa) to obtain geometrical information like beam profiles.

4.1.2. Gain

To convert the ADC counts to charge equivalents by number of released electrons, the ALiBaVa system provides an automatic gain calculation using the calibration run (see Chapter 3.2.2). As seen in Figure 4.3, the system shows linear rising at lower signals

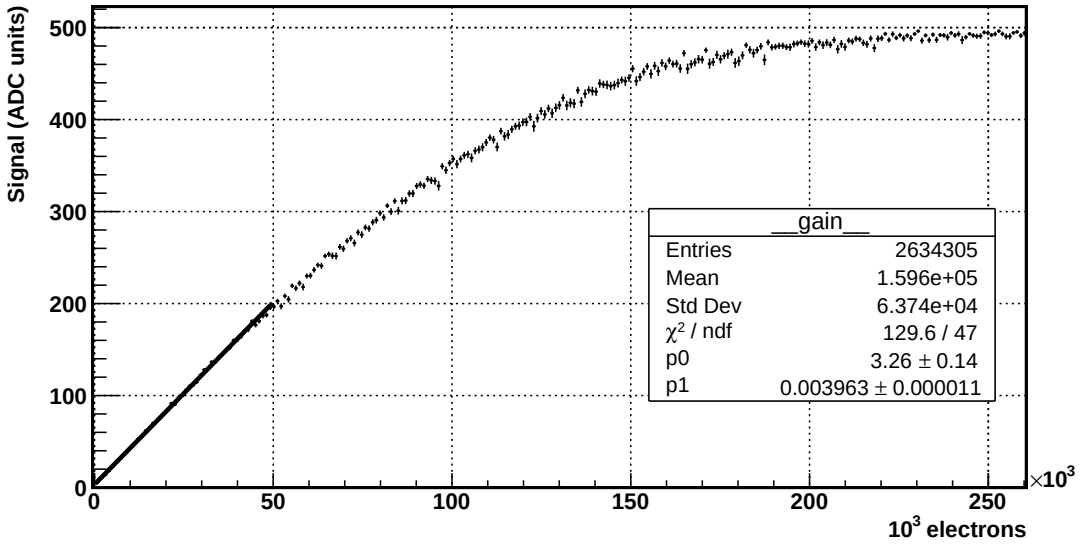

Figure 4.3.: Gain scan of MedAustron TB 2

up to $5 \cdot 10^4$ electrons, corresponding to a deposited energy equivalent of $10^5 \cdot 3.65\,\mathrm{eV}$

$\approx$ 400 keV. The energy deposition of the lowest used energy (nota bene: highest stopping power) at testbeams (nominal 62.4 MeV, with correction 33.7 MeV at TB 1, see Table 4.1) which lead to $1.7 \cdot 10^5$ electrons, corresponding to a deposited energy equivalent of 637 keV. This energy specimen is at the end of the linearity range and may be considered to be calculated manually, not by the ALiBaVa software (which uses a constant gain approximation in form of a linear ADC/charge relation). It has to be noted that usually MIPs (minimum ionizing particles; energy with minimal stopping power) are used for testbeams, whose are at approximately 2.5 GeV for protons (see 2.3), in terms of collected charge 106 electrons/µm (Kolanoski 2016[14], page 315) For an active thickness of 200 µm, $\approx 2.13 \cdot 10^4$ electrons are released. At this energy range deposited energies are lower and the linear gain approximation is legitimized.

4.1.3. Cluster analysis

Analysis of MedAustron TB 1 data revealed a discrepancy in energy deposition between NIST PSTAR data (Figure 2.3) and measured data (see Figure 4.16). After energy corrections (Chapter 4.2) there was still an offset. Due to the fact that particle rates were orders of magnitudes higher than expected, it was suspected that occupancy[c] and pile-up effects[d] were the cause of excessive energy deposition values. At high rates, single proton events were exceptions.

Analyzing cluster sizes (number of adjacent signaling strips per event) and number of

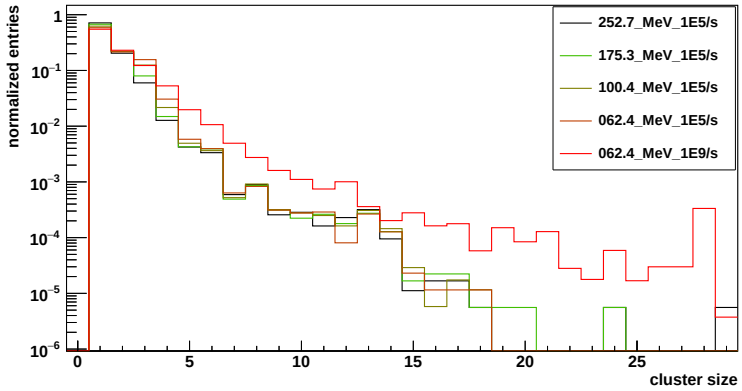

Figure 4.4.: Cluster sizes of MedAustron TB 2 at different energies and particle rates. Normalization to total number of events per run.

clusters per event and comparing them to high and low particle rates confirmed these speculations. Figure 4.4 shows cluster sizes of all MedAustron TB 2 data runs at low particle rates and on lowest energy at high rate ("062.4_MeV_1E9/s"). It makes clear that at high rates single particles cannot be time resolved reliably, significant at cluster sizes larger than 13. It has to be noted that below a probability of 10^{-4}, statistical

[c] multiple particles hitting different strips and causing multiple clusters, but counted as single hit
[d] multiple hits on the same strip resulting in signal pulse overlap

fluctuations become dominant for the low rate runs because the total number of events per run is between $1 \cdot 10^5$ and $2 \cdot 10^5$ (Table 3.4).
When looking at the first four cluster sizes in Figure 4.4, one may note that at lower energies the cluster sizes tend to be larger compared to high energies. This is explained by energy-dependent scattering distributions. At low energies, protons are more likely to be deflected at large angles, which elongates their path through the sensor and causing multiple strip hits. The number of clusters per event (Figure 4.5) confirms the evidence

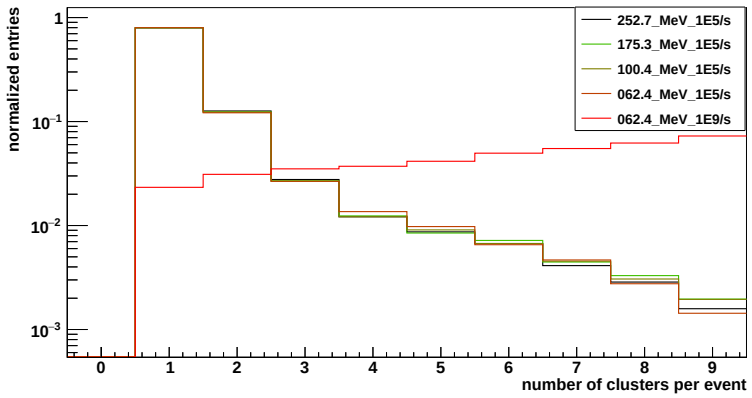

Figure 4.5.: Number of clusters per event of MedAustron TB 2 at different energies and particle rates. Normalization to total number of events per run.

for occupancy. The same high-rate run ("062.4_MeV_1E9") even shows the lowest rate of one-cluster events: Only 2.2 % of all events are one-cluster hits compared to 80 % of the low rate runs. 7 % of the events are spread out over 9 clusters, which is incompatible with the signature of single-particle hits.
On Figure 4.5 one may notice that at high particle rates the number of clusters per event are increasing at larger cluster counts, but the plot is cut at the right edge. This is caused by the ALiBaVa's analysis software, which seems to reconstruct a maximum of ten clusters per event. The same applies for the cluster size algorithm, which doesn't reconstruct clusters larger than 30.
Figures 4.6 and 4.7 illustrate a comparison of the clustering at all testbeams (TB 1, TB2 and DESY).

It has to be noted that on each testbeam, a different sensor and a different setup was used, so it can be misleading to extract correlations between these plots. However, it illustrates the differences between particle rates from highest (MedAustron TB 1 at 10^9/s) to lowest (DESY at an upper maximum of 10^3/s). The merged data runs of DESY (see Chapter3.7) covered $3 \cdot 10^6$ events in total.

4.1.4. Beam profiles

As shown in Chapter 4.2, energy loss of protons until hitting the strip sensor is dependent on initial energy. As the stopping power is higher at lower energies, one would expect to observe a Gaussian spreading of the beam, as forward scattering distribution

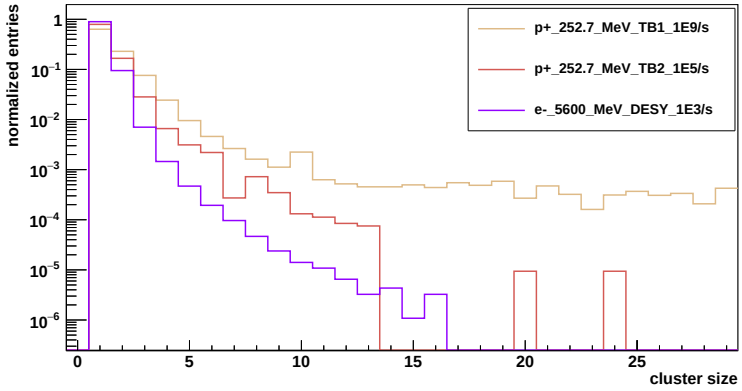

Figure 4.6.: Comparison of cluster sizes of all testbeams

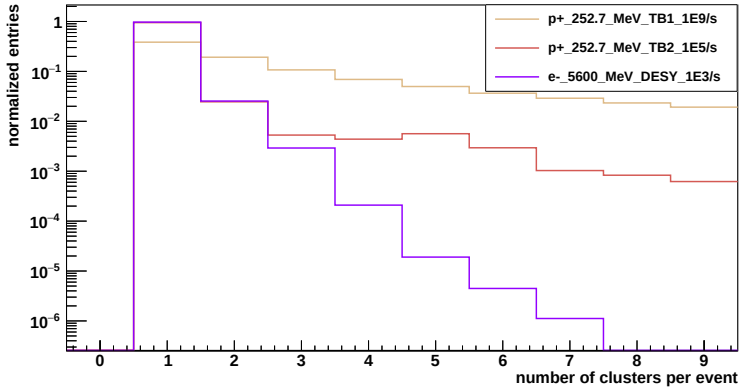

Figure 4.7.: Comparison of clusters per event of all testbeams

flattens with lower energies and higher energy transfer.

For beam profile analysis, the larger IFX Baby of MedAustron TB 1 is more suitable

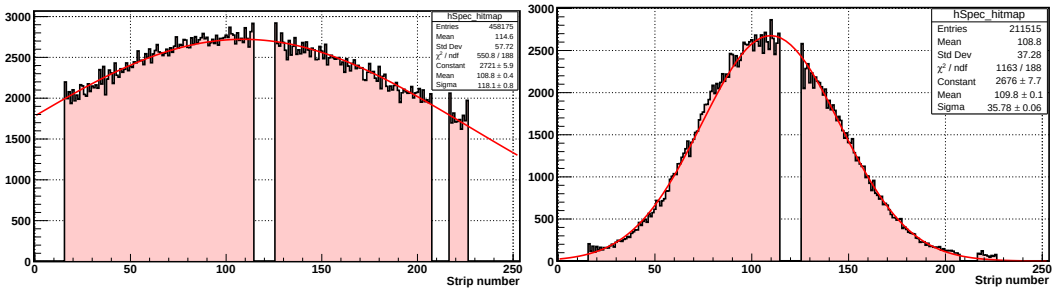

(a) Hitmap of 62.4 MeV proton beam (b) Hitmap of 252.7 MeV proton beam

Figure 4.8.: Hitmaps at two different proton energies. Results from MedAustron TB 1. At the beam center and right tail, hot channels are masked.

than the IFX Irrad of TB 2. The ALiBaVa software provides a tool for mapping the channels to the strip number as well as plotting hitmaps (total number of hits per channel/strip). Figures 4.8a and b show these hitmaps at increasing energy.

By masking out hot channels and applying Gaussian fits to the hitmaps, fit parame-

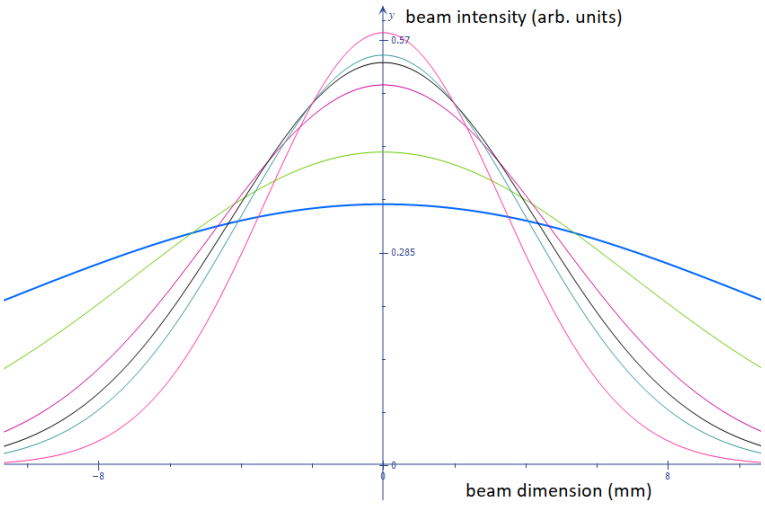

Figure 4.9.: Comparison of beam profiles of MedAustron testbeam 1

ters were obtained. Figure 4.9 shows the stacked Gaussian profiles at different energies (higher energies lead to less beam spreading) at normalized number of events. As expected, it is clearly visible that the beam widened during penetration of air, PVC and PVT layers. Unsurprisingly, this effect was reduced at higher beam energies because the scattering distribution was more forward oriented.

4.1.5. Signal histograms

Analysis of the MedAustron testbeams revealed a high noise contribution, dominant at low signals. Figure 4.10 shows two energy runs of TB 1: lowest (62.4 MeV) and highest (252.7 MeV) energy. It is clearly visible that at low energies a Landau profile (see Chapter 2.1.5) is not a good approximation anymore (as mentioned in Chapter 2.1.4), so a Gaussian profile was fitted. The left side of the signal histogram is dominated by pile-up effects and noise.

At higher energies the histograms change to Landau distributions (Figure 4.10), which permit appropriate fit parameters. Noise at the lower spectrum was removed by cutting, and a Landau distribution was fitted. Due to the fact that noise exaggerates the signal at lower ranges, the method of truncated mean (Chapter 4.3) had to be applied to calculate a robust mean value, which subsequently determined the average number of released electrons. Truncated mean (or trimmed mean) is defined by discarding given parts of a probability distribution at the high and low ends, typically by an equal amount (Kolanoski 2015[14], page 546). The peak and right hand slope of the Landau profile were distinguishable and the upper parts of the spectrum were of low noise, so fitting

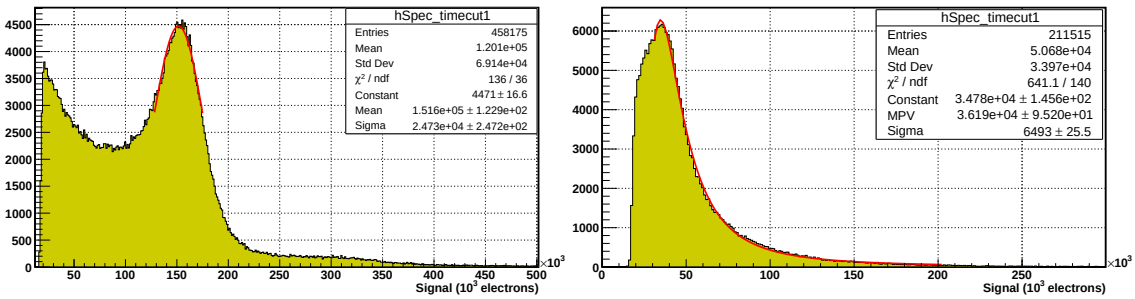

Figure 4.10.: Signal histograms of MedAustron TB 1. Left: 62.4 MeV, right: 252.7 MeV
Sensor: IFX Baby, U_{bias} = -100 V

was oriented at these parts of the distribution. After the fit, the spectrum was cut from the left side, so the mean could be calculated without being influenced by the excessive noise at the left tail.
Figure 4.11 is composed of all data runs of MedAustron TB 1. It can be observed that the Gaussian profile (black) turns to a Landau at higher energies (red). Also the signal spectrum becomes sharper defined, because higher energy protons are less prone to deceleration in matter. At the left side of the signal histogram, the distributions are superimposed by noise and pile-up effects. It has to be noted that the labeling identifies nominal energies at the accelerator outlet window, not the actual corrected at the sensor.

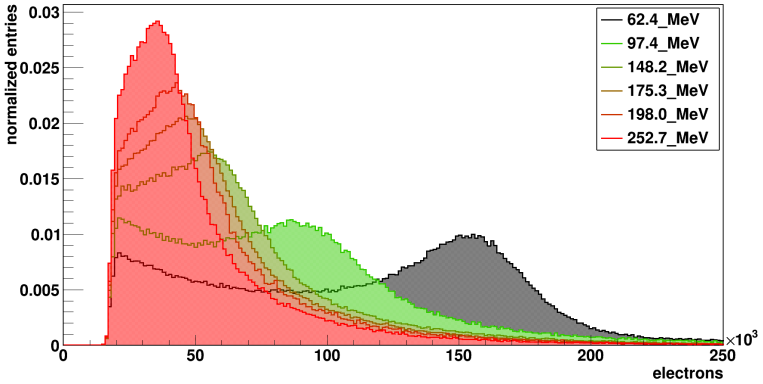

Figure 4.11.: Stacked histograms of the signal of MedAustron testbeam 1.

Figure 4.12 illustrates the signal spectrum of five merged data runs (same as in Chapter4.1.3) from the DESY testbeam. As for the Medaustron testbeams, the method of truncated mean was applied to the left flank of the distribution. The resulting mean was at $(2.65 \pm 0.43) \cdot 10^4$ electrons, which is equivalent to a deposited energy of $(2.08 \pm 0.39) \cdot 10^4$ MeV cm^2/g. It was assumed that only collision stopping power contributed to the signal, not radiative losses, because bremsstrahlung in the keV range is highly forward oriented. NIST ESTAR (Figure2.2) states a collision stopping power of

2.24 MeV cm^2/g for 5.6 GeV electrons (NIST ESTAR[15], 2018/03).
However, the usage of truncated mean is problematic because the mean value is not robust to signal cuts and should be used with caution.

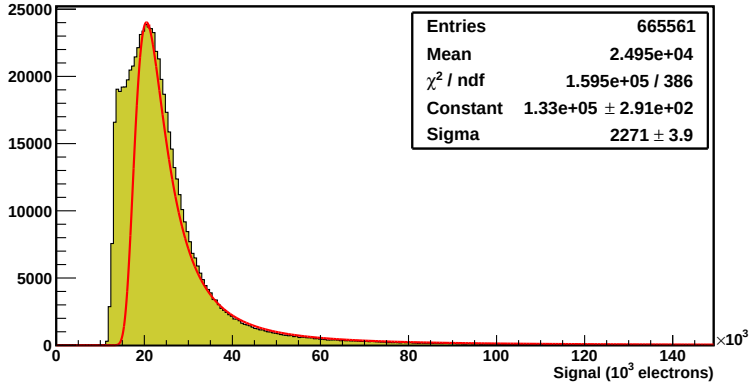

Figure 4.12.: Signal histogram of five merged runs at DESY.
Sensor: IFX CenterBias, U_{bias} = -100 V, 5.6 GeV electrons

4.2. Energy correction of MedAustron data

As seen in Figures 4.10 and 4.11, the energy profile of the lower proton energies did not follow a Landau distribution any longer. The mean ranges in silicon for these energy ranges was short enough for the detector to act as a thick absorber, so the resulting profile was Gaussian. As seen in Figure 4.13, stopping power of air and plastic at energy ranges used at MedAustron should not be neglected. Due to the scintillator thickness of 1 cm, it was expected to lose approximately 10 MeV at the lowest energy of 62.4 MeV. The stopping power of air is three magnitudes lower, but the penetrated material thickness was two magnitudes higher (60 cm). To encounter this issue, the setup of the second testbeam was changed (see Chapter 3.6).

To quantify energy losses, the simulation tool SRIM ("Stopping and Range of Ions in Matter", Ziegler 2010[29]) was used. Material budget was modeled as consecutive, homogeneous layers. Because PVT and PVC have similar and non-negligible stopping powers, the light shielding tape was also taken into account.
At TB 1, the overall presumed material budget was 50 µm polyimide (for the accelerators outlet window), 60 cm air (50 cm between beam outlet and scintillator; 10 cm between scintillator and DUT), 1 cm PVT (scintillator) and 1 mm PVC (light shieldings of scintillators and DUT). Figure 4.14 illustrates the corresponding material layers. To balance precision and run time, 1000 protons per energy run were simulated. It has to be noted that layers of similar composition were merged to single layers, because the number of layers was limited to 5 in SRIM. For a better precision, advanced simulation software like Geant4 is recommended.

At TB 2, the material budget was 50 µm polyimide (same as before), 25 cm air and

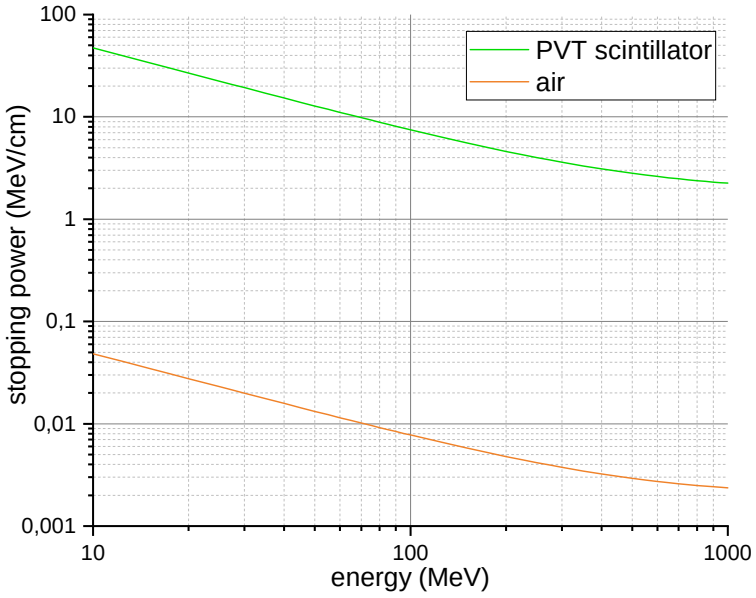

Figure 4.13.: Total stopping power for protons in polyvinyltoluene-based plastic scintillators and air (NIST PSTAR[15], 2018/02)

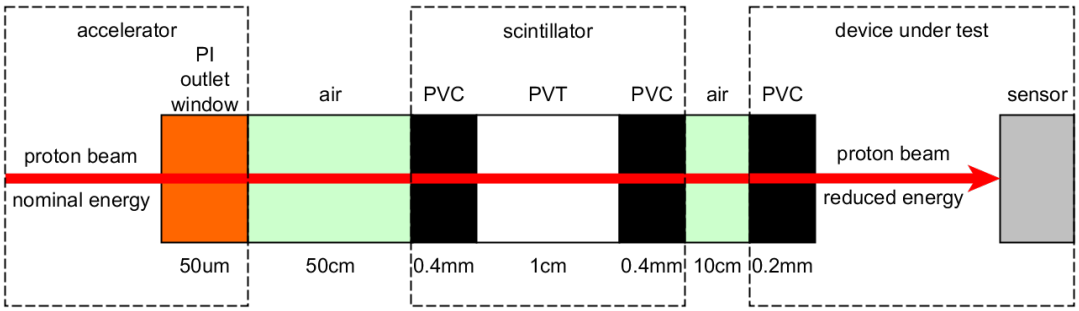

Figure 4.14.: Material budget for simulation of MedAustron TB 1 energy loss

200 µm PVC. Figure 4.15 represents the material layers. 2000 protons per run were simulated.

The resulting runs were averaged per energy, and standard deviation was calculated. Tables 4.1 and 4.2 demonstrate the outcome of the simulations. It makes clear that in terms of energy loss the TB 2 setup is superior to the TB 1, especially at low energies. The extra material layers before the sensor also lead to additional widening of the beam through scattering.

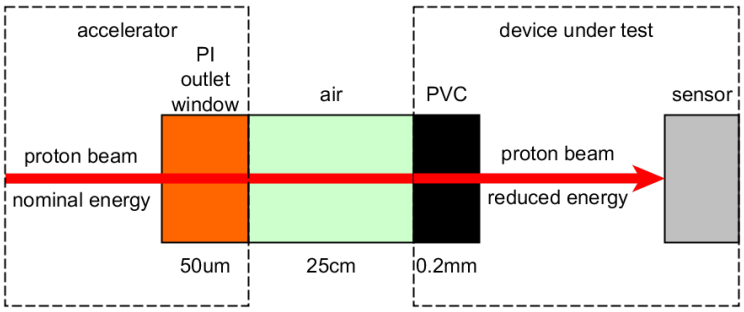

Figure 4.15.: Material budget for simulation of MedAustron TB 2 energy loss

nominal E (MeV)	**E loss (MeV)**	**E at sensor (MeV)**	**loss (%)**
62.4	28.7 ± 0.92	33.7 ± 0.92	46.0 ± 1.5
97.4	17.8 ± 0.53	79.6 ± 0.53	18.3 ± 0.5
148.2	12.6 ± 0.54	135.6 ± 0.54	8.5 ± 0.4
175.3	11.1 ± 0.56	164.2 ± 0.56	6.3 ± 0.3
198.0	10.2 ± 0.55	187.8 ± 0.55	5.2 ± 0.3
252.7	8.7 ± 0.59	244.0 ± 0.59	3.5 ± 0.2

Table 4.1.: Results of SRIM simulation for energy loss before sensor at MedAustron TB 1

nominal E (MeV)	**E loss (MeV)**	**E at sensor (MeV)**	**loss (%)**
62.4	6.1 ± 0.25	56.3 ± 0.25	9.8 ± 0.3
83.0	4.8 ± 0.26	78.2 ± 0.26	5.8 ± 0.2
100.4	4.2 ± 0.27	96.2 ± 0.27	4.1 ± 0.2
145.4	3.2 ± 0.30	142.2 ± 0.30	2.2 ± 0.1
175.3	2.8 ± 0.31	172.5 ± 0.31	1.6 ± 0.1
194.3	2.6 ± 0.33	191.7 ± 0.33	1.3 ± 0.1
252.7	2.2 ± 0.38	250.5 ± 0.38	0.9 ± 0.1

Table 4.2.: Results of SRIM simulation for energy loss before sensor at MedAustron TB 2

4.3. Stopping power determination

Due to the high noise contribution at low energy deposition scales (see Figure 4.8), fitting was focused at the right hand side of the Landau distribution. This led to the possibility for estimation of the left hand flank, to further distinguish it from noise. Multiplying the mean number of electrons with ionization energy (3.65 eV for silicon) gave the mean deposited energies. Dividing it per the active sensor thickness (thickness of the full depletion zone; 200 µm for the Infineon sensors used of the MedAustron testbeams) represents the mean energy deposition $\frac{dE}{dx}$, same as the outcome of the Bethe-Bloch formula. Dividing it by the mass density of silicon ($2.329\,\mathrm{g\,cm^{-3}}$) delivered the stopping

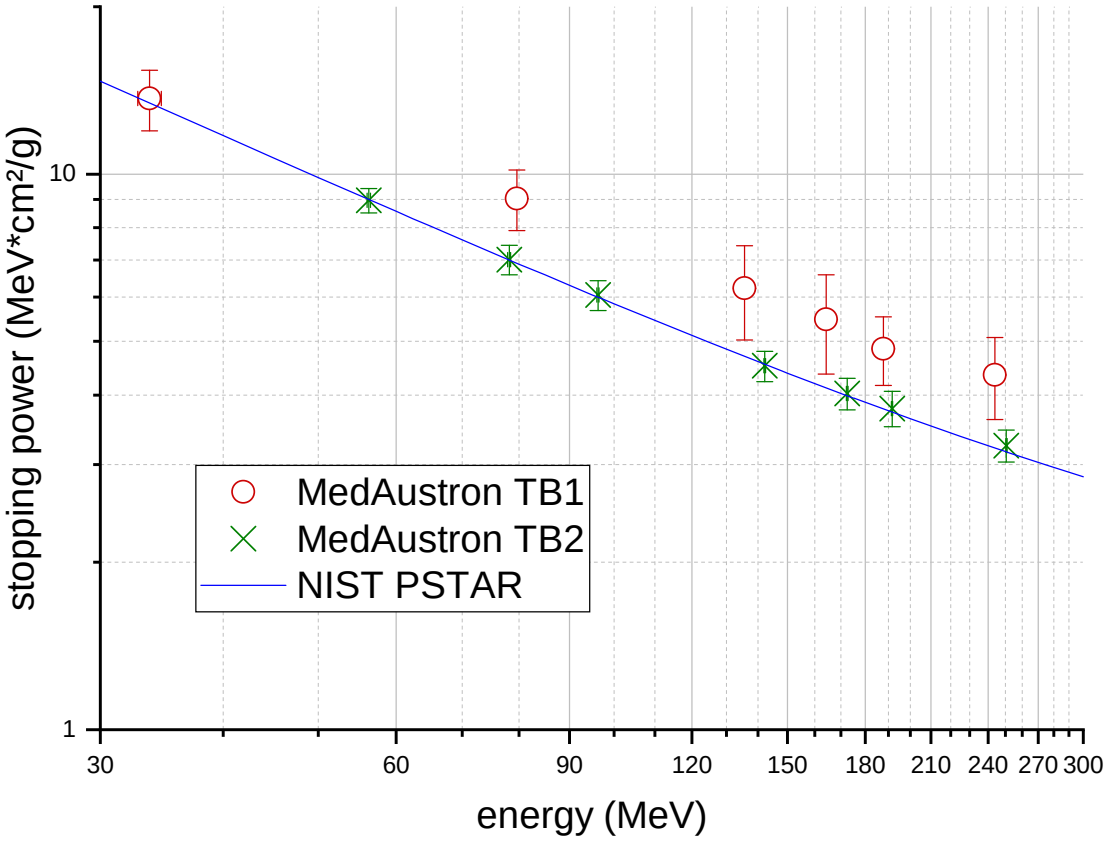

Figure 4.16.: Stopping power with energy correction of MedAustron TBs, compared to NIST PSTAR data[15]

power per density (see Figure 4.16).
It is assumed that the excessive stopping power of MedAustron TB 1 (red dots) is linked to pile-up effects[e] and occupancy (see Chapter 4.1.3). At these high particle rates, observation of the display of the bias voltage SMU via a webcam revealed that the compliance indicator LED flashed up. This lead to the conclusion that bias voltage drops during the spills reduced charge generation (by reducing the sensor's active volume through depletion zone shrink) and current flow (by reducing the electrical field). These effects were expected to partly compensate the raised energy deposition by multiple hits. The effect of bias voltage drop and subsequently reduced current pulses should be more severe at lower particle energies because of higher stopping power. This conforms to the left red dot in 4.16.
At TB 2 (green dots), the reduced particle rate didn't cause occupancy and bias voltage drops, so the stopping power showed good comparability to NIST PSTAR data[15].
The error of calculated stopping power is dominated by the fitting procedure. Pile-up

[e] overlapping pulses increase total pulse area per hit

effects, material in front of the sensor (both widened the Landau/Gauss distribution) and noise contribution at low energies impeded the identification of spectral peaks and flanks. Due to the tight time budget of 6 h of beam time per shift at MedAustron testbeams, it was difficult to obtain sufficient counts for adequate statistics at lower particle rates (TB 2). However, due to the method of truncated mean and broad cuts, peak and flank identification was possible and contributed to a lower overall error compared to TB 1. The DAQ quantization error was considered to be negligible.
The stopping power error is mainly determined by application of the fitting parameters, the energy error is dominated by simulation simplification and precision, as well as geometrical uncertainties like layer thickness and distances.

4.4. Sensor current at high rate proton beam

One of the data runs of MedAustron TB 2 was taken at high particle rate (10^9/s) at lowest energy (62.4 MeV) to maximize electron-hole pairs and therefore current consumption. Figure 4.17 shows that the currents reached up to 6.5 µA, which was 50 times IFX Irrad's idle current of 130 nA, exceeding typical compliance thresholds. This result confirmed the hypothesis that in TB 1 compliance of the bias voltage supply was reached at each spill, explaining the suppression of high signal pulses due to the effective bias voltage in the compliance situation.

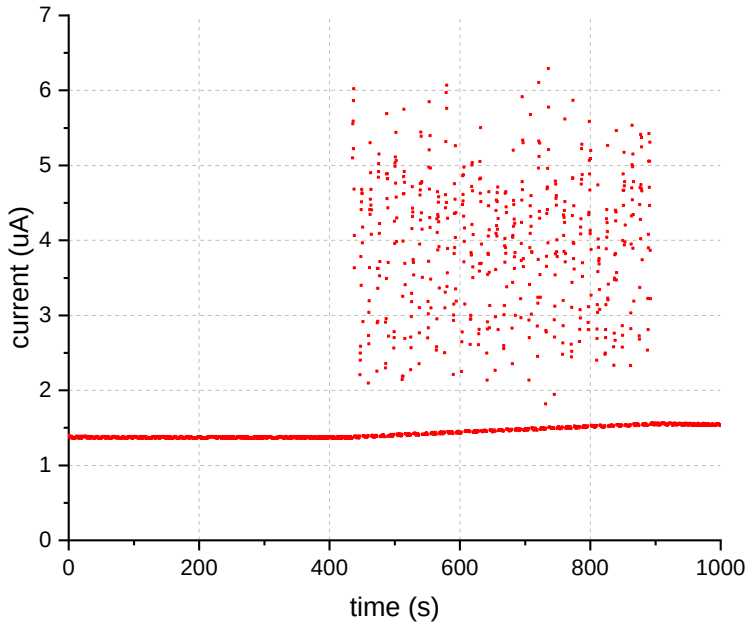

Figure 4.17.: Current consumption over time of IFX Irrad used at MedAustron TB2

5. Conclusions and Suggestions

Within the framework of this diploma thesis, the proton beam of MedAustron was used to test silicon sensors for first time. During the first testbeam (TB 1) it was observed that the compliance indicator LED of the SMU for the power supply flashed up during the spills. After the first testbeam, results of the analysis showed that high particle rates up to 10^{10}/s lead to pile-up effects and occupancy. Measured stopping power therefore was exaggerated, although it was partly compensated by the compliance of the power supply SMU, leading to a bias voltage drop which decreased charge generation and pulse currents.
To quantify the ALiBaVa's maximum processable data rate, radioactive source tests revealed that the system's maximum rate is about 600 Hz in average, but allowing bursts in the lower kHz range. This is far below particle rates at TB 1.
At low proton energies (62 MeV), the Gaussian beam profile showed an intense widening through scattering in the first scintillator and the passage through air.
Before the second testbeam, MedAustron's staff prepared, installed and tested particle rate reduction systems. At MedAustron TB 2, the setup was modified by installing all trigger scintillators after the silicon sensor to reduce energy loss of the beam. In addition, the elements were placed together as tight as possible and close to the beam outlet window. To monitor current consumption of the strip sensor, the bias supply SMU's data was read out by USB.
At TB 2, the bias supply SMU showed no indications of compliance, providing a stable voltage supply. In terms of measured stopping power, the setup of TB 2 was far superior to its predecessor. The results showed excellent conformity to reference data. Cluster analysis confirmed the reduction of occupancies at reduced particle rates of 10^5/s. For extended cluster analysis, one has to examine the behavior over the full sensor size. However, it will be necessary to modify the analysis algorithm to extend the search.
Between TB 1 and TB 2, a testbeam together with Karlsruhe Institute of Technology (KIT) was conducted at DESY. Using the electron beam (5.6 GeV) from DESY II, six sensors were tested (two from HEPHY and four from KIT). Particle rates were at approximately 200 Hz, low enough to be continuously processed by the ALiBaVa system.
All testbeams (MedAustron and DESY) exhibit high noise levels at small signal ranges, whereas this problem did not show up at the preparatory tests at HEPHY. It is assumed that this noise was caused by extrinsic factors, like focusing magnets, vacuum pumps and other control devices of the beam outlet. Modeling this noise behavior via an exponential function and subtracting it from the signal failed, so it was difficult to distinguish between noise and signal.
To circumvent the problem of noise at the lower spectrum, the method of truncated mean was successful for determining the mean value. However, the usage of this tech-

nique is problematic because the mean value is not robust to signal cuts. Due to this fact, verifications via Landau/Gauss fits are recommended.
Prospective testbeams require extensive preparations in terms of functionality tests and standardization. It is recommended to simulate the setup in advance to identify design flaws. For achieving better energy resolution in future, well-defined particle rate control is essential, as well as monitoring the current consumption of the sensor to avoid bias voltage drops. If there is a demand for low-energy beam testing, it is essential to analyze the non-linear gain behavior in the upper energy deposition range of the ALiBaVa system and extending the system's algorithm by adding an ADC-to-electrons-mapping. To make the setup resistant against RF interference, single-point grounding via copper strips prevents ground loops. It is proposed to add additional grounded shielding to the electrical components to further enhance protection against electromagnetic coupling. Maybe it will be possible to find an appropriate model to quantify electronic noise contribution to improve SNR. To measure beam profiles, the small sensor used at TB 2 was way too slim to cover the full beam distribution. Even the larger sensor of TB 1 was not sufficient, so larger strip sensors may be used for this task.
At MedAustron, short night shifts of 6 hours of beam time made troubleshooting difficult. For the next testbeams, it is suggested to conduct two or more consecutive shifts at weekends to expand active beam time, generating more data runs and improving time efficiency.

Bibliography

[1] CERN, *Organisation européenne pour la recherche nucléaire* (2017), URL http://home.cern/about/updates/2015/04/proton-beams-are-back-lhc.

[2] ILC-Collaboration, *ILC Technical Design Report* (2018), URL http://www.linearcollider.org/.

[3] CERN, *A Roadmap for HEP Software and Computing RD for the 2020s*, Tech. Rep. HSF-CWP-2017-001 (2017), URL http://cds.cern.ch/record/2298968.

[4] CMS-Collaboration, *The CMS experiment at the CERN LHC*, CERN-CMS, URL https://cds.cern.ch/record/1129810.

[5] Lippmann, C., *Particle identification*, Nucl. Instrum. Meth., A666 (2012) 148–172.

[6] Wells, P. S., *The upgraded ATLAS and CMS detectors and their physics capabilities*, Philosophical Transactions of the Royal Society of London A: Mathematical, Physical and Engineering Sciences, 373(2032), ISSN 1364-503X, URL http://rsta.royalsocietypublishing.org/content/373/2032/20140046.

[7] CMS-Collaboration, *CMS Technical Design Report for the Pixel Detector Upgrade*, CERN-CMS, URL http://cds.cern.ch/record/1481838.

[8] Friedl, M., *The CMS Silicon Strip Tracker and its Electronic Readout*, Dissertation, Technische Universitäet Wien (2011), URL http://www.hephy.at/user/friedl/diss/html/disshtml.html.

[9] CMS-Collaboration, *Observation of a new boson at a mass of 125 GeV with the CMS experiment at the LHC*, CERN-CMS, URL https://doi.org/10.1016/j.physletb.2012.08.021.

[10] CMS-Collaboration, *Technical Proposal for the Phase-II Upgrade of the Compact Muon Solenoid*, CERN-CMS, URL https://cds.cern.ch/record/2020886.

[11] CMS-Collaboration, *The Phase-2 Upgrade of the CMS Tracker*, CERN-CMS, URL https://cds.cern.ch/record/2272264.

[12] Schreiner, T., *Physics Meets Medicine* (2018).

[13] DESY, *Deutsches Elektronen-Synchrotron: DESY II* (2018), URL http://desy2.desy.de/.

[14] Kolanoski, H. and Wermes, N., *Teilchendetektoren, Grundlagen und Anwendungen*, Springer Spektrum (2016), ISBN 978-3-662-45349-0.

[15] NIST, *Physical Measurements Laboratory* (2017), URL https://physics.nist.gov/PhysRefData/Star/Text/intro.html.

[16] PDG, *Passage of particles through matter* (2007), URL http://pdg.lbl.gov/2009/reviews/rpp2009-rev-passage-particles-matter.pdf.

[17] InterAction-Collaboration, *Quantum Diaries*, URL https://www.quantumdiaries.org/.

[18] Ramo, S., *Currents Induced by Electron Motion*, Proceedings of the IRE, 27(9) (1939) 584–585, ISSN 0096-8390.

[19] Spieler, H., *Semiconductor Detector Systems*, Oxford Science Publications (2005), ISBN 978-0-19-852784-8.

[20] Grupen, C. and Buvat, I., *Handbook of Particle Detection and Imaging*, Springer Reference (2012), ISBN 978-3-642-13270-4.

[21] Hinger, V., *Charge Sharing Studies of Silicon Strip Sensors for the CMS Phase II Upgrade*, Diploma thesis, Technische Universität Wien (2017).

[22] König, A., *Electrical Characterisation and Aging Studies of Silicon Strip Sensors*, Master thesis, Universität Wien (2014).

[23] Löchner, S. and Schmelling, M., *The Beetle Reference Manual*, LHCb Electronics.

[24] ALiBaVa, *Alibava user's manual* (2018), URL https://www.alibavasystems.com/.

[25] IAEA, *Nuclear structure and decay data* (2018), URL https://www-nds.iaea.org/relnsd/vcharthtml/VChartHTML.html.

[26] Badano, L. T. and Rossi, S. C., *Characteristics of a Betatron Core for Extraction in a Proton-Ion Medical Synchrotron*, THPS048.

[27] Borburgh, J. and Kramer, T., *Design of Electrostatic Septa and Fast Deflector for MedAustron*, THPS048.

[28] DESY, *Deutsches Elektronen-Synchrotron: Telescopes* (2018), URL https://telescopes.desy.de/.

[29] Ziegler, J. F., Ziegler, M. D. and Biersack, J. P., *SRIM - The stopping and range of ions in matter (2010)*, Nuclear Instruments and Methods in Physics Research B, 268 (2010) 1818–1823, URL http://www.srim.org/.

List of Figures

1.1. Accelerators and detectors of the Large Hadron Collider 10
1.2. Run and shutdown schedule of the LHC 10
1.3. Compact Muon Solenoid 11
1.4. Particle signatures in CMS 12
1.5. Inner pixel system 13
1.6. Sketch of the prospective Outer Tracker layout of Phase-II 16
1.7. Layout of the MedAustron accelerator 16
1.8. Accelerators at DESY 18
1.9. DESY II synchrotron with test beam sites 19

2.1. Bremsstrahlung radiated from an electron 21
2.2. Mass stopping power for electrons in silicon 22
2.3. Mass stopping power for protons in silicon 24
2.4. Relative dose distribution for different particles in water 25
2.5. Energy and angular distribution ofδ-electrons 25
2.6. Gaussian profile for low energy antiprotons 26
2.7. Landau distribution 27
2.8. Schematic view on a scintillation detector system 28
2.9. Principle of a constant fraction discriminator 30
2.10. Mobility of charge carriers in silicon at 300 K 32
2.11. Drift and diffusion at a p-n junction 33
2.12. Detector diode and preamplifier 35
2.13. Schematic view of a strip sensor 36

3.1. Telescope setup for testbeams 37
3.2. Sketch of the ALiBaVa-System 39
3.3. Screenshot of the ALiBaVa GUI 40
3.4. Bad tape shielding of scintillator 1 42
3.5. Coordinate system of the scintillator tests 43
3.6. Dark rate versus radiation source rate for both scintillators 43
3.7. Geometry scans of scintillators used at MedAustron TB 1 44
3.8. Count rates at additional layers of tape 44
3.9. I-V characteristics of the sensors used at MedAustron testbeams 45
3.10. Histogram of the signal of a preparatory test run using the ^{90}Sr source . . 46
3.11. Signal histogram of laser tests at HEPHY 47
3.12. DAQ, triggering and power supply at MedAustron TB 1 49
3.13. DAQ, triggering and power supply at MedAustron TB 2 50

3.14. DAQ and triggering at DESY 52

4.1. Noise spectra of HEPHY preparatory tests and MedAustron TB 1 53
4.2. Noise per channel of MedAustron TB 2 54
4.3. Gain scan of MedAustron TB 2 54
4.4. Cluster sizes of MedAustron TB 2 at different energies and particle rates . 55
4.5. Number of clusters per event of MedAustron TB 2 at different energies and particle rates 56
4.6. Comparison of cluster sizes of all testbeams 57
4.7. Comparison of clusters per event of all testbeams 57
4.8. Hitmaps of MedAustron TB 1 57
4.9. Comparison of beam profiles of MedAustron testbeam 1 58
4.10. Signal histograms of of MedAustron TB 1 59
4.11. Stacked histograms of the signal of MedAustron testbeam 1 59
4.12. Signal histogram of five merged runs at DESY 60
4.13. Stopping power in PVT-based scintillators and air 61
4.14. Material budget for simulation of MedAustron TB 1 energy loss 61
4.15. Material budget for simulation of MedAustron TB 2 energy loss 62
4.16. Stopping power with energy correction of MedAustron TBs 63
4.17. Current consumption over time of the sensor used at MedAustron TB2 . . 64

List of Tables

1.1. LHC parameters 9
1.2. Beam parameters of the MedAustron synchrotron 17
1.3. DESY II parameters 18

2.1. Parameters of the Bethe-Bloch equation 23

3.1. Parameters of ulitized strip sensors 45
3.2. Parameters of the laser system 47
3.3. Overview of usable data runs at MedAustron TB 1 48
3.4. Overview of usable data runs at MedAustron TB 2 50
3.5. Used strip sensors at DESY 52

4.1. Energy loss before sensor at MedAustron TB 1 62
4.2. Energy loss before sensor at MedAustron TB 2 62

Glossary

ADC analog digital converter. 39–41, 54, 55, 66

APD avalanche photodiode. 28

CMS Compact Muon Solenoid. 8, 11–14, 35

CSDA continuous slowing down approximation. 23

DAQ data acquisition. 37, 38, 48–52, 64

DESY Deutsches Elektronen-Synchrotron. 5, 7, 18, 38, 45, 51, 52, 56, 59, 60, 65

DUT device under test. 38, 39, 48, 49, 51, 60

FWHM full width at half maximum. 17, 18, 48

LHC Large Hadron Collider. 8–11, 37, 39, 69

MIP minimal ionizing particle. 47, 55

MPV most probable value. 26

PDF probability density function. 26, 27

PMMA polymethyl methacrylate. 38

PMT photomultiplier tube. 14, 28, 29, 37, 48

PVC polyvinyl chloride. 58, 60, 61

PVT polyvinyl toluene. 38, 58, 60

SiPM silicon photomultiplier. 28

SNR signal-to-noise ratio. 41, 46, 66

TB testbeam. 7, 16, 30, 43, 44, 48–51, 53–66, 69, 70

TLU trigger logic unit. 38

A. Appendix

A.1. Software used for this thesis

- ALiBaVa-GUI: https://www.alibavasystems.com/
- Atom: https://atom.io/
- DESY software environment: https://telescopes.desy.de/User_manual
- SRIM-2013: http://www.srim.org/
- Web Plot Digitizer: https://automeris.io/WebPlotDigitizer/
- yEd Graph Editor: https://www.yworks.com/products/yed

A.2. Important hints for the usage of the ALiBaVa system

- Is the beam hitting all planes? Check the online Hitmap. Is there currently a spill?
- Is the sensor's power supply on?
- A crossed flat band cable between mother- and daughterboard is needed.
- Is the configuration of the Beetle chip correct? Is the latency correct? Pulse-shaping has to be activated!
- The calibration run only works if the latency is set to 128. After this, set immediately to the value appropriate for the triggering system.
- Don't forget to do frequent pedestal runs!
- Don't forget to click on "LogData"! Otherwise the data would not be saved to a file! Good practice: Save pedestals as .dat AND .ped files, via both GUI-Buttons. The .dat directly via "LogData" and the .ped via File → Save Pedestals.

A.3. Work input

For all work besides writing, a total of 1113 working hours were applied. Auxiliary work (pre-beam-tests, administrative work, planning and organizing, meetings etc.) took 195 hours. Data aquisition and analysis took 454 hours for the two MedAustron testbeams, and 464 hours for the DESY testbeam.
Writing this diploma thesis was completed in 310 hours.